



Role of the *Mycobacterium tuberculosis* ESX-4 Secretion System in Heme Iron Utilization and Pore Formation by PPE Proteins

November Sankey,^a Haley Merrick,^a Padam Singh,^a Janet Rogers,^b  Amit Reddi,^c Steven D. Hartson,^b  Avishek Mitra^a

^aDepartment of Microbiology and Molecular Genetics, Oklahoma State University, Stillwater, Oklahoma, USA

^bDepartment of Biochemistry and Molecular Biology, Oklahoma State University, Stillwater, Oklahoma, USA

^cSchool of Chemistry and Biochemistry, Parker Petit Institute for Bioengineering and Biosciences, Georgia Institute of Technology, Atlanta, Georgia, USA

ABSTRACT *Mycobacterium tuberculosis* (*Mtb*) is transmitted through aerosols and primarily colonizes within the lung. The World Health Organization estimates that *Mtb* kills ~1.4 million people every year. A key aspect that makes *Mtb* such a successful pathogen is its ability to overcome iron limitation mounted by the host immune response. In our previous studies, we have shown that *Mtb* can utilize iron from heme, the largest source of iron in the human host, and that it uses two redundant heme utilization pathways. In this study, we show that the ESX-4 type VII secretion system (T7SS) is necessary for extracellular heme uptake into the *Mtb* cell through both heme utilization pathways. ESX-4 influences the secretion of the culture filtrate proteins Rv0125 and Rv1085c, which are also necessary for efficient heme utilization. We also discovered that deletion of the alternative sigma factor SigM significantly reduced *Mtb* heme utilization through both pathways and predict that SigM is a global positive regulator of core heme utilization genes of both pathways. Finally, we present the first direct evidence that some mycobacterial PPE (proline-proline-glutamate motif) proteins of the PPE protein family are pore-forming membrane proteins. Altogether, we identified core components of both *Mtb* Heme utilization pathways that were previously unknown and identified a novel channel-forming membrane protein of *Mtb*.

IMPORTANCE *M. tuberculosis* (*Mtb*) is completely dependent on iron acquisition in the host to cause disease. The largest source of iron for *Mtb* in the human host is heme. Here, we show that the ancestral ESX-4 type VII secretion system is required for the efficient utilization of heme as a source of iron, which is an essential nutrient. This is another biological function identified for ESX-4 in *Mtb*, whose contribution to *Mtb* physiology is poorly understood. A most exciting finding is that some mycobacterial PPE (proline-proline-glutamate motif) proteins that have been implicated in the nutrient acquisition are membrane proteins that can form channels in a lipid bilayer. These observations have far-reaching implications because they support an emerging theme that PPE proteins can function as channel proteins in the outer mycomembrane for nutrient acquisition. *Mtb* has evolved a heme uptake system that is drastically different from all other known bacterial heme acquisition systems.

KEYWORDS *Mycobacterium tuberculosis*, iron acquisition, heme, type VII secretion, ESX-4, outer membrane, mycomembrane channel protein, PPE, mycomembrane, heme transport, membrane channel proteins

Mycobacterium tuberculosis (*Mtb*) has surpassed HIV/AIDS to become the leading cause of death worldwide and kills ~1.4 million people every year (1). *Mtb* is completely dependent on iron acquisition to successfully colonize the human host. During any infection, the host immune response can limit iron availability by complexing iron within ferritin or by removing iron with transport proteins such as transferrin (Tf) and lactoferrin (Lf), which are then stored in the form of heme (2–4). However, *Mtb*

Editor Craig D. Ellermeier, The University of Iowa

Copyright © 2023 Sankey et al. This is an open-access article distributed under the terms of the [Creative Commons Attribution 4.0 International license](https://creativecommons.org/licenses/by/4.0/).

Address correspondence to Avishek Mitra, avi.mitra@okstate.edu.

The authors declare no conflict of interest.

Received 15 November 2022

Accepted 16 January 2023

overcomes iron limitations by employing different iron acquisition mechanisms. To acquire iron from host Tf, ferritin, and Lf, *Mtb* secretes siderophores (5, 6), which are crucial for sequestering ferric iron. However, these siderophores cannot sequester iron from heme, which stores >75% of host iron (7).

In previous studies, our group (8, 9) and others (10, 11) have shown that *Mtb* utilizes heme as an iron source. Unlike other bacterial pathogens (12), *Mtb* employs novel mechanisms to capture and utilize heme. While Gram-negative pathogens use canonical β -barrel outer membrane proteins (OMPs) to capture/transport heme (12), *Mtb* instead uses cell surface PPE (proline-proline-glutamate motif) proteins (9, 13), which are found in the mycomembrane (mycobacterial outer membrane). In most pathogens, heme uptake through multiple cell surface receptors converges at an ABC transporter located in the cytoplasmic membrane (12). *Mtb* employs multiple independent pathways to transport heme across the cytoplasmic membrane. We showed that *Mtb* has at least two redundant pathways, where the genetic requirements for heme utilization (8) can be significantly altered in the presence of serum albumin. The existence of this albumin-dependent heme utilization pathway is perhaps not surprising. Since albumin strongly binds heme and is the most abundant protein in blood (14), it is likely that *Mtb* utilizes the albumin pathway for heme acquisition when blood is available. Remarkably, a very similar albumin-dependent heme acquisition mechanism has also been observed in *Candida albicans* (15). While these observations highlight how *Mtb* has evolved to employ unique mechanisms to acquire the essential iron micronutrient, they also demonstrate the significant gaps in our understanding of the basic underlying mechanisms of *Mtb* heme acquisition.

In this study, our primary objective was to identify unknown components of *Mtb* heme acquisition. Herein, we show that the ancestral ESX-4 type VII secretion system (T7SS) is required for efficient heme utilization. *Mtb* has five T7SS (ESX1-5). ESX-1, 3, and 5 are the most well-characterized systems playing important roles in *Mtb* virulence or iron acquisition or being essential, respectively (16). A unifying theme of ESX-1, 3, and 5 is that export of many *Mtb* PPE proteins is dependent on these systems. In contrast, ESX-2 and ESX-4 are the least studied and their functions had not been identified. Phylogenetic analysis shows that ESX-4 is the most ancestral T7SS from which all other ESX systems evolved through genetic duplication (17). In this study, we identified that the culture filtrate proteins Rv0125 and Rv1085c are required for *Mtb* heme utilization and their export is dependent on an intact ESX-4 secretion system. Furthermore, we identified that the alternative sigma factor SigM is necessary for heme utilization and is potentially a global activator of heme utilization genes. Finally, we show that some mycobacterial PPE proteins that bind heme are also channel-forming OMPs. *Mtb* PPE proteins were originally hypothesized to function in antigenic variation (18, 19), but there is an emerging hypothesis that some PPE proteins can also function as channel proteins required for nutrient uptake. Our observations provide the first direct evidence for this hypothesis.

RESULTS

Identification of the *Mtb* heme regulon. *Mtb* strain H37Rv was grown to the mid-exponential phase in liquid albumin-free iron-free 7H9 (7H9_{Fe}) containing either 10 μ M ferric citrate (FeCi) or 10 μ M heme as the sole iron source, and then we analyzed the transcriptome by RNAseq to identify genes upregulated in response to heme. Our analysis revealed that a total of 181 genes were upregulated more than 2-fold with statistical significance in heme (Fig. 1A). Interestingly, a previous study by Rodriguez et al. (20) showed that 37 (20%) of these 181 genes (Table S1 in the supplemental material) are also induced under low iron conditions. Of these 37 genes, ~57% (21) of these genes encode proteins for siderophore biosynthesis (*mbt* genes) (22), siderophore export (*mmpS4/L4/S5*) (23, 24), and siderophore import (*irtA/B*) (25–27), which are not required for heme utilization. The other 16 genes encode proteins for metabolism, putative transcriptional regulators, and proteins of unknown function. Of these low iron-induced

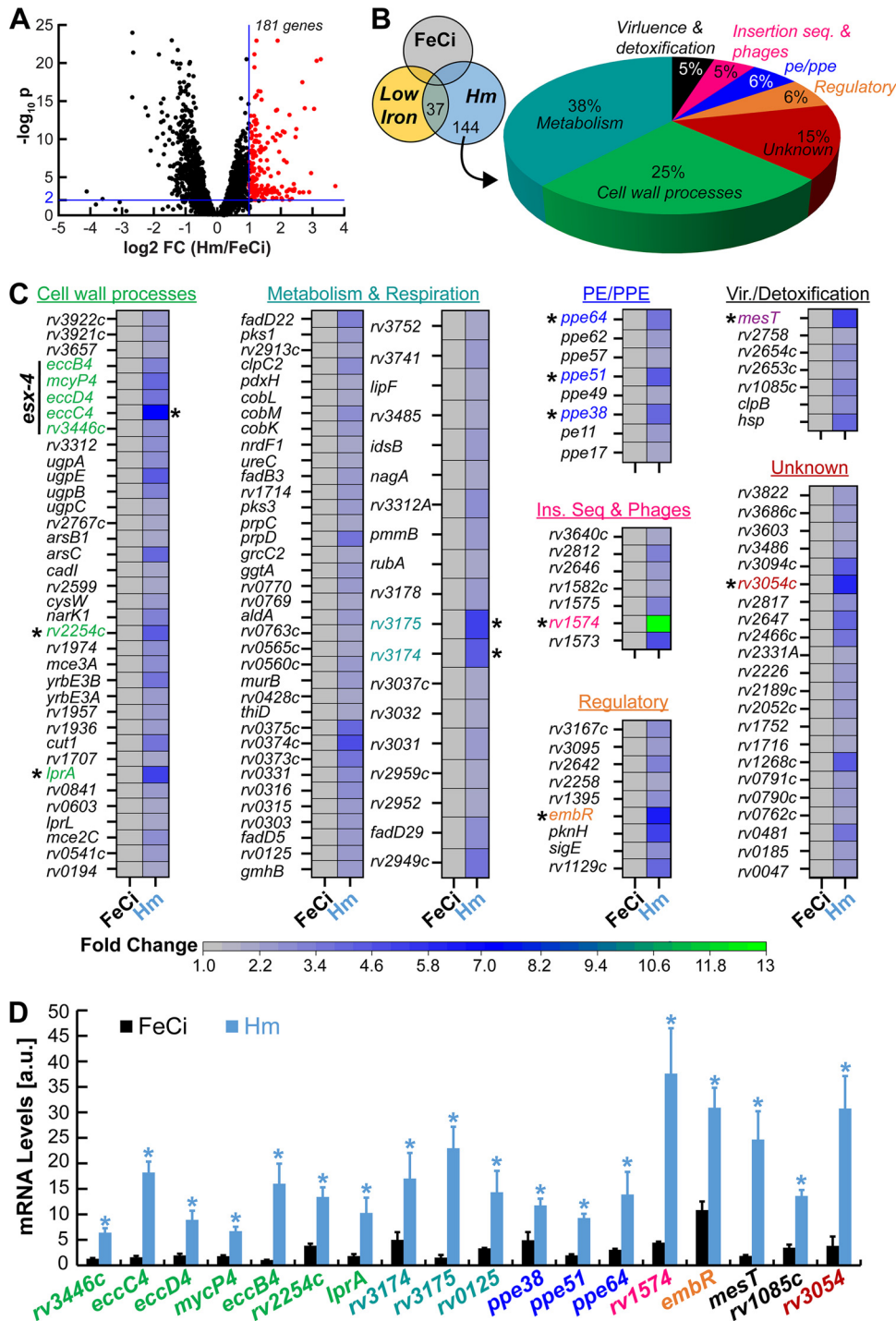


FIG 1 Transcriptomic analysis of *Mycobacterium tuberculosis* (*Mtb*) and identification of the heme regulon. (A) Volcano plot analysis between heme (Hm) and ferric citrate (FeCi) conditions where $-\log_{10} q$ values are plotted against \log_2 fold change (FC) for each genetic locus. Nonaxial vertical line denotes ≥ 2 -FC of 182 genes in heme while the nonaxial horizontal line denotes the significance threshold ($q < 0.01$). (B) Category of genes that are upregulated in Mtb by >2 -fold in heme compared to low iron and FeCi. (C) Heat map representing FC of the 144 heme-specific genes compared to FeCi. Light gray color of the FeCi column represents FC of 1.0 and is the same for all genes. Genes shown with asterisks were selected for validation by quantitative real-time PCR (qRT-PCR). (D) Expression levels of selected genes in FeCi or heme (Hm) determined by qRT-PCR. Error bars represent standard error of mean (SEM) values of biological triplicates; a.u., arbitrary units. Asterisks denote gene expression is significantly different in heme, compared to FeCi. Statistical significance was determined by Tukey's honestly significant difference (HSD) following an F test ($P < 0.05$). Source data file is provided.

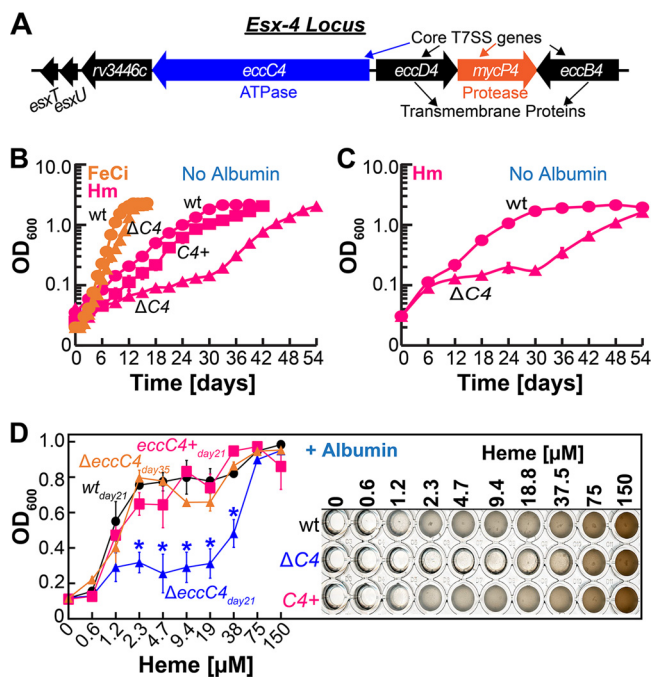


FIG 2 Effect of *Mtb* ESX-4 disruption on heme and albumin-heme utilization. (A) Schematic representation of the *Mtb* *esx-4* locus genes. (B to D) Growth of wt (circles), $\Delta eccC4$ ($\Delta C4$, triangles), and complement ($C4+$, squares) strains. (B) Growth of strains in albumin-free iron-free 7H9 containing 10 μ M FeCi (orange) or 10 μ M heme (pink). (C) Growth of stationary-phase cultures of $\Delta eccC4$ from day 54 (Fig. 2B) inoculated into fresh albumin-free iron-free 7H9 medium containing 10 μ M heme. (D) Growth of strains in liquid iron-free 7H9 containing 0.5% albumin and various concentrations of heme determined by measuring endpoint OD_{600} on day 21. Growth experiments were performed in 96-well plates ($n = 3$), where a representative image is shown on the right after 21 days of growth. Image of 96-well plate on day 35 is shown in Fig. S1D. Asterisks denote significant differences for $\Delta eccC4$ compared to wt or complement strains. Statistical significance was determined by Tukey's HSD following an *F* test ($P < 0.05$). All heme medium contains 50 μ M 2'-2'-dipyridyl (DIP) to prevent utilization of trace iron. All error bars represent SEM of biological triplicates. In many cases, error bars are smaller than marker data points. Source data file is provided.

genes, we also observed upregulation of *ppe37*, which was shown to be required for heme utilization in *Mtb* Erdman (13) but not in *Mtb* H37Rv as we demonstrated in our previous study (8). Aside from these low iron inducible genes, we identified an additional 144 genes that were upregulated in the presence of heme (Table S1; Fig. 1B and C). A significant number of these genes encode proteins for cell wall processes (25%), cell and lipid metabolism (38%), and proteins of unknown function (15%). Expression of 8 genes encoding canonical PPE and PE (proline-glutamate motif) proteins, which are known to be cell surface associated, were increased >2 -fold in heme. Specifically, we observed heme-dependent upregulation of *ppe62* (Fig. 1A; Table S1), which we have shown in our previous study to be required for *Mtb* heme (Hm) utilization (9). This is in line with our previous observations and supported the experimental conditions used in this study. The other 22% of the genes encode proteins for virulence and detoxification, insertion sequence and phages, and putative transcriptional regulators. To validate our RNAseq data, we picked genes with the highest expression from each category (Fig. 1C, asterisks) and measured their mRNA levels by quantitative reverse transcriptase PCR (qRT-PCR). Expression levels of all selected genes were significantly upregulated >2 -fold in heme compared to just the FeCi condition, validating our transcriptomic analysis (Fig. 1D). Altogether, our transcriptomic screen identified a heme regulon, which also includes genes that are part of the general iron stress response of *Mtb*.

ESX-4 is required for efficient heme iron utilization by *Mtb*. Our transcriptomic analysis showed that the genes in the ESX-4 locus, encoding components of a T7SS (Fig. 2A), were upregulated in the presence of heme, which we verified by qRT-PCR (Fig. 1D). To determine if ESX-4 is required for *Mtb* heme utilization, we constructed an

unmarked deletion mutant of *eccC4* (Fig. S1A to C), which encodes the ATPase-energizing protein for ESX-4 secretion. First, we analyzed the growth of wild-type (wt) and $\Delta eccC4$ in 7H9_{-Fe} containing either FeCi or heme. All heme media in our study contained 50 μ M 2'-dipyridyl (DIP) as an iron chelator to prevent trace iron utilization. Strains were always iron depleted before inoculation into the test medium. The growth of both strains is similar in FeCi reaching the stationary phase by day 12 (Fig. 2B). Heme iron utilization by *Mtb* is slower, and wt reaches the stationary phase by day 30 (Fig. 2B). Deletion of *eccC4* significantly delayed growth in heme with a long lag phase, and $\Delta eccC4$ starts growing exponentially around day 30. Growth impairment of $\Delta eccC4$ was recovered to near wt levels by complementation upon production of EccC4 from the chromosomally integrated expression vector pOAL102 (Table S3). The abrupt growth of $\Delta eccC4$ around day 30 (Fig. 2B) hinted a suppressor mutation could be allowing recovery. If this was the case, we hypothesized that harvesting $\Delta eccC4$ cells from the stationary phase and then inoculating them into fresh heme medium would allow the mutant to grow faster or at a similar rate as wt. Inoculation of stationary phase $\Delta eccC4$ from heme medium (day 54) into fresh heme medium shows that $\Delta eccC4$ still exhibits the growth delay (Fig. 2C) demonstrating that the growth recovery of $\Delta eccC4$ is not due to a suppressor mutation.

We also determined the ability of $\Delta eccC4$ to utilize albumin heme by growing strains in iron-free 7H9-albumin (7H9A_{-Fe}) containing various concentrations of heme and measuring endpoint optical density at 600 nm (OD₆₀₀). After 21 days, the growth of the *eccC4* mutant was significantly impaired compared to the wt and complement strains except at very high Hm concentrations (Fig. 2D). By day 35, $\Delta eccC4$ grew to wt levels (Fig. 2D; Fig. S1D) similar to the growth recovery observed in albumin-free heme (Fig. 2). As a solely qualitative approach, we visually examined the growth of strains by plating on self-made iron-free 7H10-albumin solid agar plates (7H10A_{-Fe}). In the absence of any iron, wt and $\Delta eccC4$ showed residual amounts of growth (Fig. S1F). Both strains grew similarly with FeCi (Fig. S1G), but in the presence of Hm (Fig. S1H) growth of $\Delta eccC4$ was delayed compared to the wt and complement strains. Since cell permeability can affect the transport of hydrophobic molecules such as Hm, we determined cell permeability in $\Delta eccC4$ by monitoring the uptake of ethidium bromide. EtBr uptake rates were similar in both strains (Fig. S1E) suggesting that the heme growth defect is not due to altered cell permeability. Collectively, these results demonstrate that disruption of the ESX-4 system reduces the efficiency of *Mtb* heme utilization through both pathways.

ESX-4 is required for heme uptake in *Mtb*. ESX-4 could be involved in heme uptake by transporting heme into the cytosol or ESX-4 could be involved in heme efflux by exporting heme out of the cytosol to maintain heme homeostasis. Lack of uptake would result in the absence of iron nutrients for the cell and lack of efflux could result in intracellular heme accumulation and toxicity. Either mechanism could result in the growth defect observed in $\Delta eccC4$. To differentiate these two hypotheses, we used a heme biosensor that directly responds to intracellular levels of heme.

We utilized the HS1-M7A biosensor, which consists of a heme-binding domain of cytochrome b₅₆₂ conjugated to red (mKATE) and green (eGFP) fluorescent proteins (28, 29). In the presence of heme, heme binding by the b₅₆₂ domain quenches green fluorescence. The red fluorescence is always unaffected and serves as a useful internal standard to account for any various protein levels. The biosensor level is always reported as a green/red ratio. In the absence of heme, there is no heme binding by b₅₆₂, green fluorescence is not quenched, and the green/red ratio is higher. Thus, we hypothesized that if ESX-4 functions in Hm uptake, then $\Delta eccC4$ will have lower levels of Hm relative to wt and green/red ratio in $\Delta eccC4 >$ wt. If ESX-4 functions in Hm efflux, then $\Delta eccC4$ will have higher levels of Hm relative to wt and green/red ratio in $\Delta eccC4 <$ wt. In a recent study, the Reddi group (30) demonstrated that the HS1-M7A biosensor is functional in *Mtb*. As such, we constructed the HS1-M7A mycobacterial episomal expression vector pOAL311, which expresses *hs1-M7A* from the constitutively active *psmyc* promoter (31). pOAL311 was transformed into

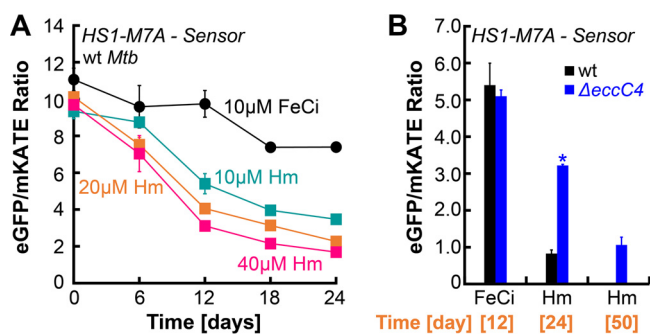


FIG 3 Response of intracellular heme biosensor in *Mtb*. (A) Temporal response of HS1-M7A intracellular biosensor to either 10 μM FeCi (circles) or various concentrations of heme (Hm, squares) in wt *Mtb*. (B) Temporal response of HS1-M7A biosensor to either 10 μM FeCi or 10 heme in *Mtb* (black) or ΔeccC4 (blue). Heme medium contained 50 μM DIP to prevent utilization of trace iron. Error bars represent SEM of three biological replicates. In many cases, error bars are smaller than marker data points. Asterisks denote significant differences for ΔeccC4 compared to wt at the specific time point. Statistical significance was determined by Tukey's HSD following an F test ($P < 0.05$). Source data file is provided.

Mtb and biosensor fluorescence was monitored temporally. The fluorescence ratio of the biosensor was quenched in the presence of heme in a heme dose-dependent manner demonstrating that the biosensor functioned in *Mtb* as shown before (Fig. 3A). Next, we examined biosensor fluorescence in wt and ΔeccC4 . In FeCi, the fluorescence ratio is unchanged between wt and ΔeccC4 (Fig. 3B). However, in heme, the fluorescence ratio in ΔeccC4 is 3-fold higher compared to wt at day 24 suggesting significantly lower levels of heme in ΔeccC4 , and then by day 50, the fluorescence ratio reached wt levels suggesting increased heme levels. Collectively, these results suggested that ESX-4 enabled heme uptake.

ESX-4 does not affect PPE36 or PPE62 protein localization. Previously, we demonstrated that PPE36 and PPE62 are two cell surface proteins required for efficient heme utilization (9). Since the export of many PPE proteins requires T7SS in *Mtb* (17), we hypothesized that disruption of ESX-4 could affect PPE36/62 export and subsequently heme utilization. We determined the subcellular localization of PPE36 and PPE62 by performing membrane fractionation experiments as we did previously (9). Fractionation experiments showed that PPE36/62 localization is unchanged in ΔeccC4 (Fig. S2) indicating that ESX-4 does not affect PPE36/62 export.

Rv0125, Rv1085c, and SigM are required for heme utilization. While performing our heme growth analysis for wt and ΔeccC4 in albumin-free 7H9 medium, we observed that after 30 days of growth, the culture supernatant from wt Hm medium displayed a brown-red color compared to the green color in ΔeccC4 (Fig. 4A). Free Hm in solution has a green color and shifts to brown-red upon complexation by proteins. This suggested that Hm is complexed within some protein(s) in wt *Mtb* that were absent or in low abundance in ΔeccC4 . Thus, we hypothesized that the ESX-4 system could be influencing the export of some culture filtrate protein(s) that is required for heme utilization. FeCi and heme supernatants were harvested for both wt and ΔeccC4 strains as described in Methods. Culture filtrate proteins were isolated, and by mass spectrometry, we identified 2,615 proteins in both strains (Table S2). A comparison of protein levels showed that in ΔeccC4 the levels of 1,173 proteins (Fig. 4B; Table S2) and 335 proteins (Fig. 4C; Table S2) were altered in FeCi and heme, respectively. We then focused on identifying proteins whose levels were reduced at least 2-fold or greater in ΔeccC4 . We found that levels of 61 proteins (Fig. 4B; Table S2) and levels of 74 proteins (Fig. 4C; Table S2) were reduced >2 -fold in FeCi and heme, respectively. We then used the Tuberculist (32) database to categorize proteins that were identified in *Mtb* culture filtrate in previous studies. Through this process, we identified that in ΔeccC4 levels of 3 proteins were reduced in both FeCi and heme culture filtrate. The levels of 5 proteins were reduced only in FeCi, and 6 were reduced specifically in heme (Fig. 4D). Additionally, our proteomic analysis showed that levels

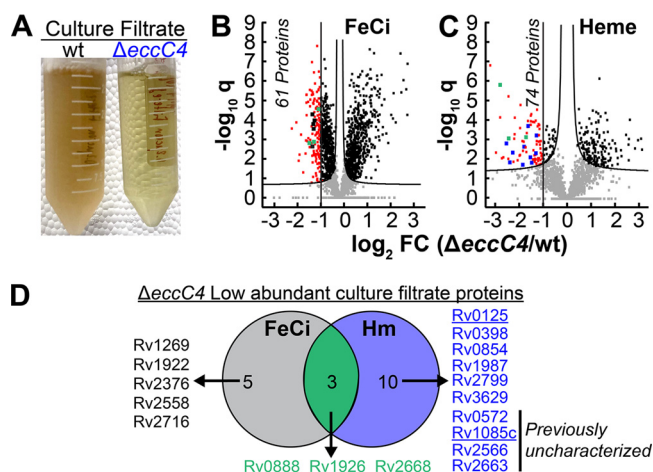


FIG 4 Proteomic analysis of culture filtrate protein in wild-type *Mtb* and $\Delta eccC4$ strains. (A) Visual analysis of culture supernatant of wt and $\Delta eccC4$ strains from heme medium at day 30. Picture is of heme cultures of strains on day 30 used for growth experiments in Fig. 2B. (B and C) Perseus SAM volcano plot analysis illustrating abundant proteins in wt compared to $\Delta eccC4$ in FeCi (B) and heme (C) conditions. The $-\log_{10} q$ values are plotted against $\log_2 FC$ for each protein. Nonaxial vertical line denotes ≥ 2 -FC of protein levels in $\Delta eccC4$ wt compared to wt. Asymptotic curves denotes the significance threshold ($P < 0.05$). Differentially expressed proteins with statistical significance are colored. (D) Venn diagram illustrating known and unknown culture filtrate proteins identified to be in low abundance in $\Delta eccC4$. Unique FeCi or heme (Hm) proteins in low abundance in $\Delta eccC4$ are shown colored in black dots (in panel B) and blue dots (in panel C), respectively. Rv0125 and Rv1085c underlined in blue were also identified in RNAseq analysis (Fig. 2D). Proteins in low abundance in $\Delta eccC4$ under both conditions are shown in green dots (in panels B and C). Source data file is provided.

of 4 proteins, which have not been previously characterized, were also reduced in the heme culture filtrate.

Out of the 10 heme-specific proteins, the genes encoding Rv0125 and Rv1085c were also identified to be upregulated in wt *Mtb* (Fig. 1D) suggesting possible roles in *Mtb* heme utilization. We first constructed isogenic marked deletion mutants (Fig. S3) and then inoculated strains in medium with various iron sources and compared growth by measuring endpoint OD₆₀₀. With FeCi, all mutants displayed similar or higher levels of growth compared to wt (Fig. 5A). In albumin-free heme, deletion of *rv0125* reduces growth to 30 to 40% ($P < 0.05$), but at heme concentrations $>10 \mu M$, there is no difference in growth compared to wt (Fig. 5B). Deletion of *rv1085c* reduces growth in heme from ~ 60 to 70%, and in heme concentrations $>40 \mu M$, the growth difference is abrogated (Fig. 5C). To ensure that the growth defects were specific to the gene deletion, we constructed $\Delta rv0125$ - and $\Delta rv1085c$ -complemented strains by expressing the corresponding genes from the chromosomally integrated expression vectors pOAL319 and pOAL320, respectively (Table. S3). The growth of both mutants was recovered to wt levels upon complementation with the respective gene (Fig. 5B and C).

Previous studies have shown that the alternative sigma factor SigM acts as a transcriptional activator of *esx-4* locus genes (33, 34). Since ESX-4 is required for heme utilization, we hypothesized that SigM may also be required for heme utilization. We constructed a marked *sigM* deletion mutant (Fig. S3) and analyzed its growth as we did for *rv0125* and *rv1085c*. Deletion of *sigM* does not affect *Mtb* growth in FeCi (Fig. 5A) but significantly reduces growth in heme (Fig. 5D). Compared to the *rv0125* and *rv1085c* mutants, the *sigM* mutant exhibits considerably reduced growth in heme, which could be recovered to wt levels by expressing *sigM* from the chromosomally integrated expression vector pOAL321 (Table. S3). We next examined if SigM is required for activating *esx-4*, *rv0125*, or *rv1085c* by measuring gene expression. As expected, expression of all *esx-4* operon genes was significantly reduced anywhere from 2 to 4-fold in $\Delta sigM$ (Fig. 6). Expression of *rv0125* and *rv1085c* was unaffected in $\Delta sigM$ suggesting that SigM does not affect heme utilization by directly regulating

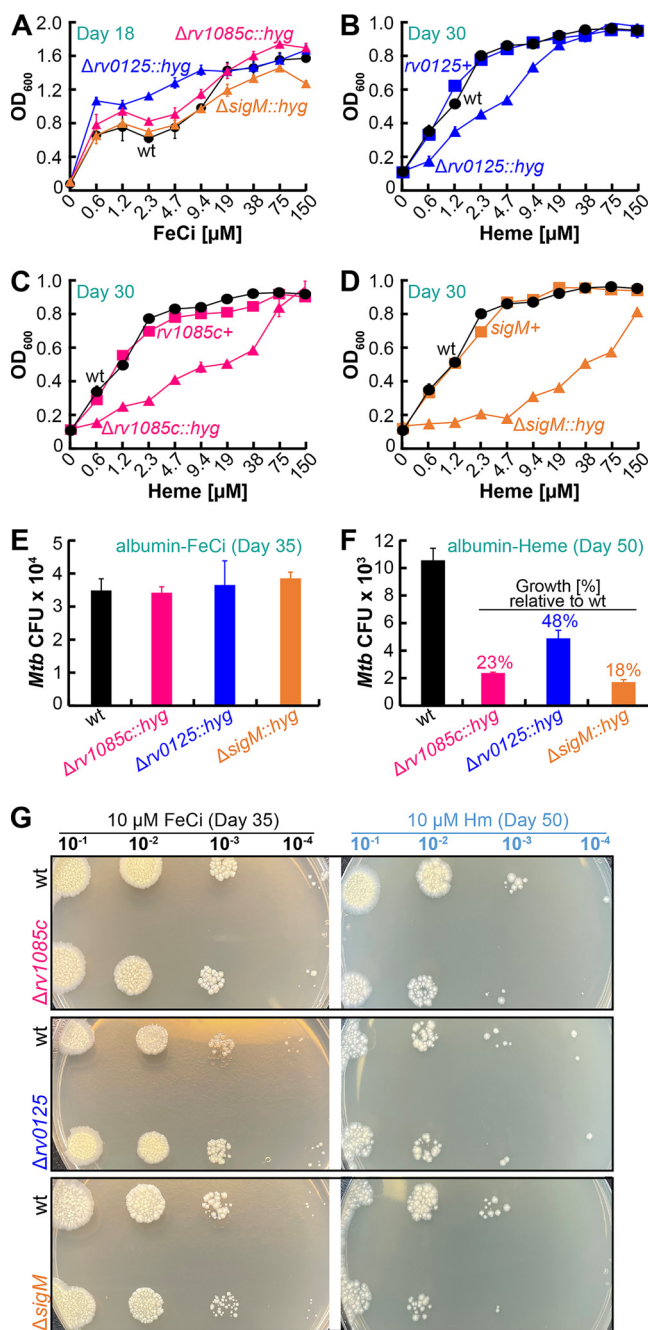


FIG 5 Growth of wt *Mtb* and mutant strains. (A to D) Growth of wt (black circles), mutants (colored triangles), and complement strains (colored squares). Growth was determined by measuring endpoint OD_{600} in liquid albumin-free iron-free 7H9 containing increasing concentrations of FeCi (A) at day 18 or heme (B to D) at day 30. Note: wt data points in panels B to D are the same. (E and F) Growth of strains determined by spotting dilutions on iron-free 7H10-albumin plates containing 10 μ M FeCi on day 35 (E) or 10 μ M heme on day 50 (F). CFU counts were determined from either 10^{-3} or 10^{-4} dilution. (F) Percent values show relative growth of mutant compared to wt. (G) Shows a representative image of agar plates used to determine CFU counts shown in panels E and F. All error bars represent SEM of biological triplicates. In many cases, error bars are smaller than marker data points. Source data file is provided.

transcription of *rv0125* and *rv1085c*. We also determined the ability of all mutants to utilize albumin heme by analyzing growth on solid agar plates (Fig. 5G). With FeCi, all mutants grew similarly as wt (Fig. 5E). As observed in nonalbumin heme growth (Fig. 5B to D), all mutants displayed significantly reduced growth in the presence of albumin heme (Fig. 5F). The *rv1085c* and *rv0125* mutants displayed ~23% and 48%

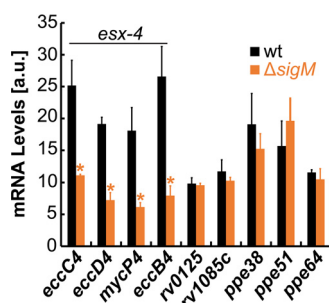


FIG 6 Effect of *sigM* deletion on gene expression. Expression levels of genes in wt (black) and $\Delta sigM$ (orange) grown in iron-free 7H9 medium containing 10 μM heme determined by qRT-PCR. Asterisks denote significant differences for $\Delta sigM$ compared to wt. Error bars represent SEM of biological triplicates. In many cases, error bars are smaller than marker data points. Statistical significance was determined by Tukey's HSD following an *F* test ($P < 0.05$). Source data file is provided.

growth compared to wt, whereas $\Delta sigM$ displayed $\sim 18\%$ growth compared to wt. Collectively, our results show that Rv0125, Rv1085c, and SigM are required for efficient heme utilization through both heme utilization pathways.

PPE64 can bind heme and form channels in a lipid bilayer. Our transcriptomic analysis showed that the genes encoding PPE38, PPE51, and PPE64 (Fig. 1D) were highly upregulated in heme. Since we have shown that some PPE proteins can bind heme (9), we first determined if these heme-upregulated PPE proteins can bind heme. Recombinant PPE64_{6His} (Fig. 7A), PPE51_{6His} (Fig. S4A), and PPE38_{6His} (Fig. S4E) were produced within inclusion bodies (IB) in *E. coli* and then purified by nickel chromatography under denaturing conditions. Removal of urea from the solution by dialysis caused proteins to rapidly precipitate, which could only be prevented in the presence of a detergent in the solution, suggesting that these PPE proteins are indeed membrane proteins. Urea was dialyzed, and PPE64_{6His} (Fig. 7B), PPE51_{6His} (Fig. S4B), and PPE38_{6His} (Fig. S4F) were refolded in the presence of 0.5% *N*-octyl-oligo-oxethylene (OPOE) or 0.1% *n*-dodecyl- β -D-maltoside (DDM). We next examined the distribution of the refolded proteins by size exclusion chromatography (SEC) by loading equal amounts of each protein sample. With DDM, PPE64 (Fig. 7C) and PPE51 (Fig. S4C) were refolded into variable species showing the presence of aggregates and different oligomeric forms. In contrast with OPOE, PPE64 (Fig. 7D) and PPE51 (Fig. S4D) display a more uniform distribution. While PPE38 displayed a more uniform distribution in DDM (Fig. S4G) compared to OPOE (Fig. S4H), the DDM refolded proteins levels were significantly lower as observed by absorbance at 280 nm. The presence or absence of proteins in all SEC fractions for all proteins was confirmed by SDS-PAGE.

We next determined the heme binding capability of proteins by difference absorption spectroscopy. The heme spectra were subtracted from heme-protein spectra to determine the presence of the characteristic Soret peak at ~ 410 nm, indicative of protein-heme binding. We first used MhuD and IdeR as positive- and negative-control proteins, respectively. These proteins were purified as we did before (9), and MhuD shows the characteristic Soret peak, which is absent in IdeR (Fig. 8A). Analysis of all fractions of PPE51 (2, 9, 18, 19, 21, 35–37) (Fig. S6C and D) and PPE38 (6, 9, 14, 15, 21, 38) (Fig. S6G and H) did not show any heme binding (data not shown). However, like MhuD, only PPE64_{OPOE} fraction 14 (Fig. 7E) showed absorbance at 410 nm indicating that it binds heme (Fig. 8A). PPE64-heme binding was also validated by surface plasmon resonance (SPR) spectroscopy as we did previously (8, 9). The addition of heme to PPE64 resulted in a dose-dependent increase in signal intensity indicating heme binding (Fig. 8B). Since the export of many PPE proteins to the cell surface requires T7SS in *Mtb* (17), we determined if the export of PPE64 requires ESX-4. Thus, we determined if the cell surface accessibility of PPE64 was affected by ESX-4 disruption. *Mtb* cells expressing C-terminally HA-tagged PPE64 were harvested for the detection of protein on the whole-cell surface by flow cytometry as we did previously (9). SpmT_{HA} (surface

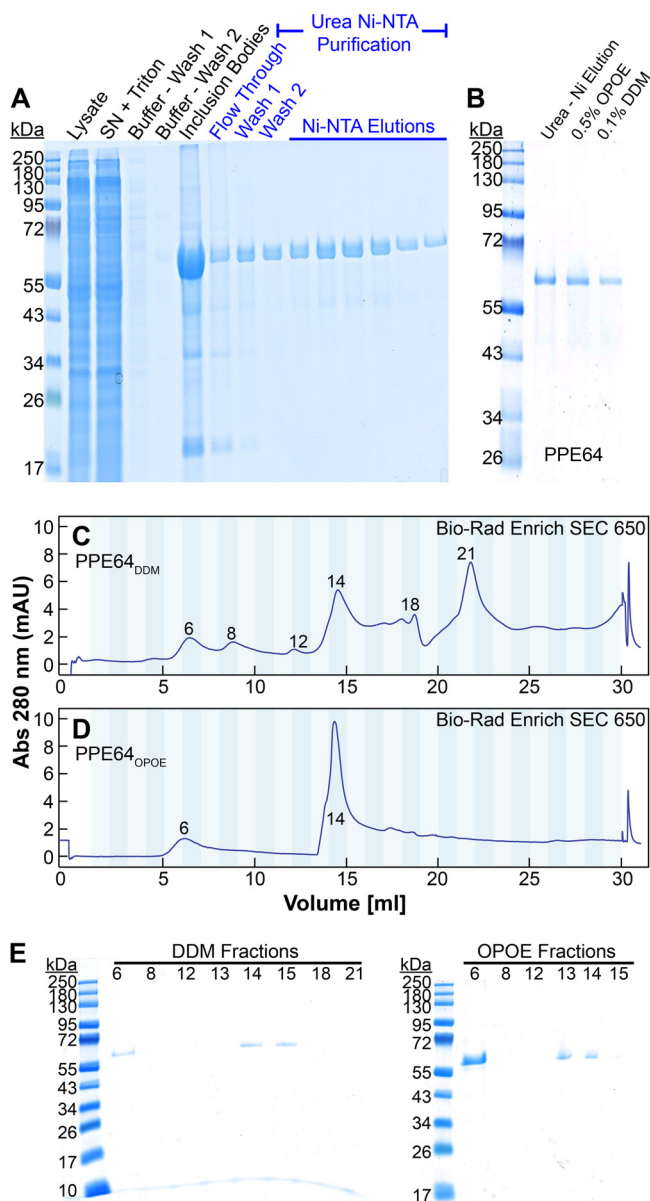


FIG 7 Purification of PPE64. (A) Recombinant PPE64_{6His} was purified from inclusion bodies using nickel affinity chromatography under denaturing (8 M urea) conditions. (B) Urea was dialyzed and recombinant PPE64_{6His} was then refolded in the presence of 0.5% OPOE or 0.1% DDM. (C and D) Analysis of refolded PPE64_{DDM} (C) or PPE64_{OPOE} (D) by size exclusion chromatography (SEC) using Bio-Rad Enrich SEC 650 column. Flow rate, 1 mL/min; fraction volume, 1 mL. Numbers within chromatogram show fraction number. (E) Analysis of SEC fractions by SDS-PAGE.

protein) and MbtG_{HA} (inner membrane protein) were used as positive and negative controls, respectively. SpmT_{HA} was detected on the cell surface in wt and Δ eccC4 and MbtG_{HA} detection only showed background levels of fluorescence in both strains (Fig. 8C). Cells expressing PPE64_{HA} (Fig. 8C) showed a very similar shift in signal and levels of fluorescence in both wt and Δ eccC4. Altogether, our data suggest that PPE64 is a cell surface heme-binding protein and its export is not dependent on an intact ESX-4 system.

Our previous studies and others have hypothesized that cell surface PPE proteins can function as channel proteins for the transport of nutrients (8, 9, 39, 40). Since PPE64 is a heme-binding cell surface protein, we analyzed the pore-forming capability of PPE64 by monitoring protein insertion and channel formation in a lipid bilayer

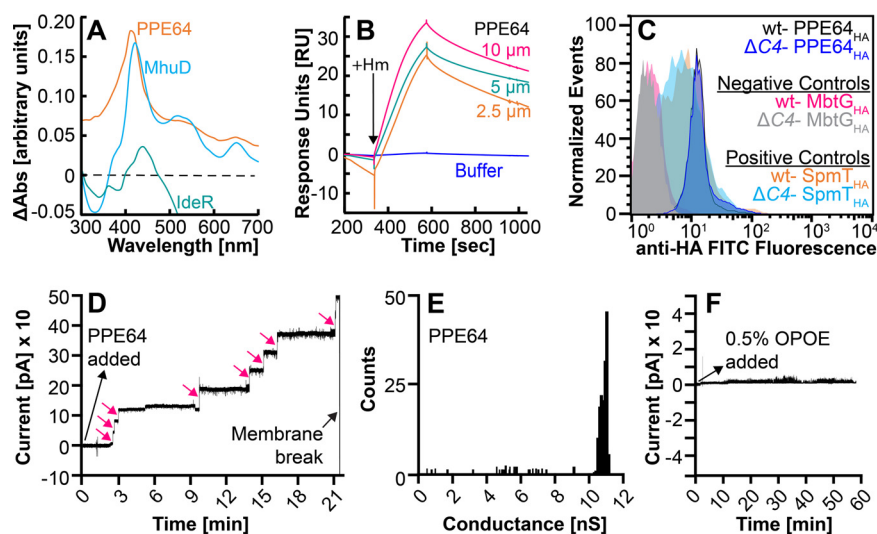


FIG 8 Characterization of PPE64. (A) Detection of heme binding by PPE64 through difference absorption spectroscopy. Free heme spectra were subtracted from heme-incubated protein spectra at protein concentrations of 10 μ M. Spectroscopy experiments were performed a minimum of three times. (B) Heme binding by PPE64 at various heme concentrations determined by surface plasmon resonance (SPR) spectroscopy. (C) Surface accessibility of PPE64_{HA} in wt and Δ c4 strains determined by flow cytometry. MbtG_{HA} (inner membrane protein) and SpmI_{HA} (outer membrane protein) were used as negative and positive controls, respectively, for surface accessibility in both strains. Source data file is provided. (D and F) Channel-forming activity of PPE64 in planar lipid bilayers. PPE64 refolded in OPOE detergent buffer was added to diphytanoyl phosphatidylcholine (DphPC) membranes with 30 mV applied potential. Current trace was recorded for PPE64 (D) and OPOE buffer (F). For panel D, each stepwise increase (pink arrows) in current trace represents a channel formation in the lipid bilayer. (E) Histogram of single-channel conductance for PPE64 collected from 5 membranes. A total of 37 pores were analyzed. The average single-channel conductance was $\sim 11 \pm 0.3$ nS. Source data acquisition files (axon binary files) are too large for upload and require pClamp software for viewing. Data files will be provided upon request.

through electrophysiology experiments. Using diphytanoyl phosphatidylcholine (DphPC) lipids, a lipid membrane was formed in the aperture of a Delrin cup, and the baseline current trace was monitored (Fig. S5A). We first validated our lipid bilayer setup using the control protein MspA (41), which is the most abundant porin in *M. smegmatis*. MspA (Fig. S5F) was selectively heat extracted as described before (42) and rapidly formed channels in the bilayer (Fig. S5C). These channels showed an average channel conductance of $\sim 4.2 \pm 0.5$ nS (Fig. S5D), which is in line with the reported conductance for wt MspA (43) demonstrating that our bilayer setup functions appropriately. To examine channel activity for PPE64, ~ 40 ng of protein was added to the *cis* compartment and the current trace was temporally monitored. All PPE64 fractions (Fig. 7C and D) from size exclusion chromatography were analyzed, but only PPE64_{OPOE} fraction 14 (Fig. 8D) led to a stepwise increase in the current trace with an average channel conductance of ~ 11 nS ± 0.3 (Fig. 8E), indicating that PPE64 actively inserted into the lipid bilayer and formed channels. To control for any buffer effect, OPOE buffer was added to the bilayer, which did not show any change in the current trace (Fig. 8F) or channel activity proving that the channel activity was PPE64 specific. Since PPE proteins have a highly conserved N-terminal domain (18, 19), it could be that the channel activity is a general property of all PPE proteins. To address this, we purified PPE36_{6His} (Fig. S5E) as we did before (9) and analyzed its channel-forming capability. PPE36 (Fig. S5B) did not form any channels showing that the channel activity is specific to PPE64 and also not due to any indirect effect from the 6 \times His tag. Our observations show that PPE64 functions in pore formation *in vitro* and argue for similar roles *in vivo*.

DISCUSSION

Previous studies have identified roles for the ESX-4 T7SS in *M. smegmatis* (34, 44), *M. abscessus* (45), and *M. marinum* (46, 47). More recently, in two separate studies, it

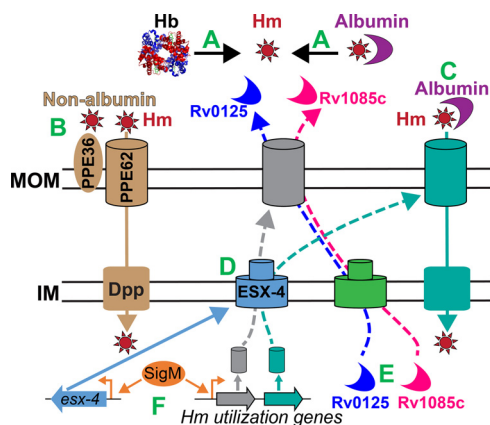


FIG 9 Model for *Mtb* heme utilization. (A) Heme (Hm) uptake invariably starts with removal of heme from host hemoproteins. (B) In the nonalbumin pathway, PPE36/62 functions at the cell surface, and the Dpp transporter functions at the inner membrane. (C) In another pathway, heme uptake is influenced by the presence of serum albumin. (D) The ESX-4 T7SS is involved in exporting proteins to the cell surface or extracellular milieu that are necessary for both pathways. (E) Rv0125 and Rv1085 are required for heme utilization and their export is somehow dependent on ESX-4. Rv0125/Rv1085 are likely not direct substrates of ESX-4 because they do not contain any ESX signal sequences. (F) SigM directly controls activation of *esx-4* genes and/or other unknown heme utilization genes but does not regulate expression of *rv0125* or *rv1085c*. PPE64 is an outer membrane heme binding channel protein in *Mtb* and is not shown in the model because its role in heme utilization has yet to be determined experimentally.

was shown that ESX-4 affects the export and localization of the CpnT exotoxin in both *Mtb* and *M. marinum* (46, 48). Our study presents the exciting new finding that the ancestral ESX-4 T7SS is also necessary for efficient heme iron utilization through both *Mtb* heme utilization pathways (Fig. 9). The requirement of ESX-4 in heme utilization is not absolute because the *eccC4* mutant eventually reaches wt levels of growth. In *M. marinum*, it has been shown that there is cross-talk between ESX-4 and other T7SS such as ESX-1 and ESX-5 (47). Thus, it is possible that another T7SS compensates for ESX-4 allowing $\Delta eccC4$ to grow in heme. We found that *esx-3* operon genes, encoding the ESX-3 T7SS, were upregulated in the presence of heme (Table S1). It is known that ESX-3 is required for siderophore-mediated iron acquisition (49–52). Therefore, ESX-3 could be functioning as a backup system for heme utilization in the absence of ESX-4. However, this raises the question of why this compensation would take ~ 30 days to activate in $\Delta eccC4$ (Fig. 2D) for growth recovery. We also observed that numerous low-iron responsive genes (20, 53) were also upregulated in heme (Table S1). Since heme iron utilization in *Mtb* is less efficient than ferric-siderophore utilization, the induction of siderophore biosynthesis and export/import may represent a general response to slow heme iron utilization. Alternatively, the DIP iron chelator, which is membrane permeable, could be chelating some intracellular iron resulting in the activation of low iron-responsive genes in the heme medium. A reasonable argument can be made that differences in the cell permeability of wt and $\Delta eccC4$ could affect DIP uptake into cells exacerbating the growth phenotype seen in $\Delta eccC4$. However, cell permeability of $\Delta eccC4$ is unchanged and as such any intracellular iron chelating effects of DIP likely remain the same in both wt and $\Delta eccC4$.

By using the HS1-M7A intracellular biosensor, we show that cytosolic heme levels in wt *Mtb* reach an equilibrium around 24 days. This is reflective of the fact that the growth rate of *Mtb* is slower in heme than that in ferric iron (Fig. 2A) (8–10). Our biosensor data show that ESX-4 affects heme uptake into the cytoplasm. ESX-4 does not uptake heme directly because all T7SS systems (17) function unidirectionally to export substrates across the cytoplasmic membrane. The likeliest scenario is that ESX-4 influences the export of protein(s) to the mycomembrane or extracellular milieu that are necessary for heme uptake. We demonstrated that ESX-4 does not affect the export of PPE36 and PPE62, two cell surface proteins that are required for heme utilization.

Based on our observation of the distinct color of the wt and $\Delta eccC4$ heme culture filtrate, we hypothesized that some heme utilization-specific protein(s) was absent in $\Delta eccC4$. In our analysis of heme culture filtrate proteins, we expected to find the proteins EsxU and EsxT as control proteins for ESX-4 secretion (Fig. 2A). EsxUT is ESAT-6/CFP-10-like proteins and genes encoding these types of proteins are found in all T7SS locus (54). The EsxUT homologs EsxAB, EsxGH, and EsxMN are secretion substrates of their cognate T7SSs Esx-1, Esx-3, and Esx-5, respectively. Since ESX-4 is involved in heme utilization and EsxUT is part of the ESX-4 locus, we expected to observe varied EsxUT levels in the wt and $\Delta eccC4$ heme culture filtrate. However, EsxUT was not detected under any condition in any strain in our proteomic analysis. An important point to note is that EsxAB, EsxGH, and EsxMN all have the canonical WxG and YxxxD/E type 7 secretion signal motifs. In these heterodimeric complexes, the WxG motif in one partner protein with the YxxxD/E motif in the other partner forms a bipartite type 7 recognition signal. Most importantly, the YxxxD/E motif and the 3 amino acid spacing between Y and D/E are essential for the recognition and secretion of these substrates through their cognate T7SSs (55). Even the Esx homologs in firmicutes require the WxG and HxxxD/ExxhxxxH motifs for secretion through their type 7B systems (56). While EsxU has the WxG motif, there is no YxxxD/E motif in EsxT. It has been suggested that EsxUT is the primary secretion substrate of ESX-4, but previous studies in *Mtb* and *M. smegmatis* have only examined *esxUT* gene expression through sigma factor overexpression (57, 58) and *esxUT* gene transcript levels in the context of mycobacterial distributive conjugal transfer (34, 44). While EsxUT secretion has been observed in *M. abscessus* (*Mab*), it should be noted that the *Mab* EsxT homolog contains the HxxxD/ExxhxxxH motif necessary for secretion (59). To surmise, we do not actually know if EsxUT is secreted in *Mtb*, which may explain why EsxUT was not detected in our proteomic analysis.

Our proteomic analysis showed that ESX-4 disruption decreased levels of Rv0125c and Rv1085c in the heme culture filtrate, whose corresponding genes were also identified to be upregulated in *Mtb* in the presence of heme. Rv0125 and Rv1085c are very likely not directly exported by ESX-4 because they do not contain any ESX recognition sequences (60, 61). It is more likely that ESX-4 controls the export of some other unknown protein(s) to the mycomembrane, which affects the extracellular transport of Rv0125 and Rv1085c (Fig. 9E). In an unpublished (62) proteomic analysis, the *M. smegmatis* Rv1085c homolog (Msmeg_5257) was also found to be in lower abundance in an *esx-4*_{Msmeg} mutant supporting our proteomic analysis. We recognize that we did not directly examine the protein levels of Rv0125 and Rv1085c in wt and $\Delta eccC4$, but based on the proteomic and transcriptomic precedence, we opted to characterize *rv0125* and *rv1085c* by mutational analysis and found both mutants to be partially defective in heme utilization. Rv0125 is a putative (Tuberculist) secreted trypsin-like serine protease. The active site of the trypsin serine proteases has three catalytic residues (S195, H57, and E102) (63), and Rv0125 contains similar residues S195, H57, and E113 in its predicted active site. Moreover, Rv0125 also shares sequence similarity with the secreted hemoglobin serine protease Hbp of *E. coli* O157:H7, which contains very similar active site residues (S207, H73, and E101) (64–67). Hbp is an autotransporter (68–70) (975 aa, ~112 kDa) consisting of a β -barrel translocator domain and a passenger domain. The passenger domain contains the protease activity that releases/binds heme by degrading hemoglobin (64, 71). Rv0125, a much smaller protein (355 aa, ~35 kDa), does not contain a translocator domain and only shares sequence similarity (33%) with the Hbp passenger domain. Thus, we hypothesize that Rv0125 may function similarly in binding and capturing heme from hemoglobin and then delivering the heme to a cell surface receptor.

Rv1085c is predicted to be a hemolysin-like protein based only on sequence similarity with hemolysins from other bacteria (Tuberculist). There is clear precedence for hemolysin function in iron utilization because bacterial pathogens use them to disrupt erythrocytic membranes to release hemoglobin to use as an iron source (72). Rv1085c

is also predicted to have 7 α -helical transmembrane domains, and a reasonable argument can be made that it could be a cytoplasmic membrane protein further raising the question of why it would be present in the culture filtrate. There are two explanations for this observation. First, many pore-forming proteins of the colicin and cytolysin family also share this feature. For example, monomers of Colicin A (PDB: 1COL), which contains 10 transmembrane helices (73, 74), are first released in a soluble form that subsequently assembles into a higher-order oligomeric structure (75). Thus, it is common for pore-forming proteins such as hemolysins to contain α -helical hydrophobic helices which are commonly found in transmembrane proteins. Second, the presence of Rv1085c in culture filtrate can also be explained in the context of mycobacterial extracellular vesicle (MEV) production. It is well established that various iron/medium compositions (76) and host environments (77, 78) lead to MEV production of a different composition. For example, under iron-limiting conditions, *Mtb* releases MEVs containing the lipidic siderophore mycobactin as a mechanism to acquire ferric iron (76). MEVs are also loaded with lipids (79) that are found in the cytoplasmic membrane, which has led to the conclusion that MEVs originate from the cytoplasmic membrane. This was further corroborated by MEV proteomic analysis (80) showing that the majority of proteins are lipoproteins and proteins belonging to the cell wall, membrane function, and intermediate metabolism and respiration. A key point is that MEVs are secreted in the culture supernatant and are typically isolated using 100-kDa cutoff ultrafiltration units. In our study, we used a 3-kDa cutoff ultrafiltration unit to concentrate the whole culture filtrate, and as a result our analysis detected several of the previously identified MEV proteins (Table S2). Since heme induces *rv1085c* expression and iron availability changes MEV composition, it is conceivable that Rv1085c is released within MEVs as a mechanism of heme acquisition from host erythrocytes. This could explain why Rv1085c was found in the culture filtrate. Altogether, in our model (Fig. 9), we predict that Rv1085c may be required to lyse erythrocytes to release hemoglobin, which is then degraded by Rv0125 to release and capture heme.

We also discovered that a *sigM* mutant has a pronounced growth defect in heme (Fig. 5). This is unsurprising given that SigM is known to activate expression of the *esx-4* genes *esxT*, *esxU*, *eccC4*, and *mycP4* (57, 58). One observation is that all *esx-4* locus genes except *esxU* and *esxT* were upregulated in heme in our study. Previous studies have shown that *esxUT* expression is increased upon SigM overproduction (57, 58). Since we show that SigM and ESX-4 are required for heme utilization, we expected *esxUT* to be similarly increased as the other *esx-4* genes. There are some possible explanations for this discrepancy. First, expression analysis of *esxUT* and other *esx-4* genes in *Mtb* was primarily performed upon overproduction of SigM because native expression/level of *sigM*/SigM is not enough to induce *esx-4* genes. Second, these overexpression studies also showed that transcript levels of *esx-4* genes, which are organized in two divergent operons, are very different suggesting that there are multiple levels of regulation (transcriptional/posttranscriptional) that we do not fully understand. Third, the activation of *esx-4* genes without any overexpression to the best of our knowledge has only been observed in *M. smegmatis* (34, 44). Thus, the very different growth conditions of our study may explain why we did not observe increased *esxUT* expression in heme. Moreover, unchanged gene expression does not necessarily mean unchanged protein levels as EsxUT protein levels could very well be elevated by posttranslational mechanisms. Since deletion of *sigM* only reduced the expression of *esx4* genes (Fig. 6) but did not eliminate their expression, this suggests that SigM may act as an activator of other unknown heme utilization genes beyond the *esx-4* locus (Fig. 9F). Since SigM is required for both heme utilization pathways, this gives us the first potential handle to identify components of the albumin-heme pathway. A future direction of exploration will be to examine the transcriptomic profile of $\Delta sigM$ to identify genes specifically expressed in albumin heme. While these findings help us improve our understanding of *Mtb* heme utilization (Fig. 9), clearly further experimentation is needed to determine the exact mechanisms of how ESX-4, Rv0125, Rv1085c, and SigM function in *Mtb* heme utilization.

Our transcriptomic analysis showed that the genes encoding PPE38, PPE51, and PPE64 were significantly upregulated in heme. This was significant because in our previous studies we showed that some *Mtb* PPE proteins are required for heme utilization (9). We determined that recombinant PPE38 and PPE51, which were extracted and refolded from inclusion bodies, do not exhibit any heme binding. This suggests that these proteins either do not bind heme or maybe they are in a folded state that does not support heme binding. Clearly, further experimental work with native proteins and through mutational analysis is necessary to determine if these proteins have any role in heme iron utilization. However, we identified that PPE64 is a cell surface protein (Fig. 8C) and demonstrated using two spectroscopy approaches that it binds Hm (Fig. 8A and B). These observations are perhaps not entirely surprising because PPE64 shares 57% sequence (Fig. S6) similarity with PPE62, which we showed is also a cell surface protein that binds heme and is required for heme utilization (9). Since deletion of *ppe62* only partially affects *Mtb* heme utilization, it is possible that PPE64 could be a redundant functioning partner of PPE62. We fully recognize that a drawback in our study is that we have yet to determine if PPE64 contributes to *Mtb* heme utilization through mutational analysis. However, an exciting finding of our study is that PPE64 is a channel-forming membrane protein as demonstrated through lipid bilayer analysis (Fig. 8E and F). To the best of our knowledge, this is the first direct evidence of channel activity by a PPE protein. Using PPE36 and MspA as negative and positive controls, respectively, we showed that PPE64 actively forms channels in a lipid bilayer (Fig. 8E and F). The channel conductance of PPE64 is ~ 11 nS, which is vastly different from other mycobacterial channel proteins such as MspA (~ 5 nS) (43), MctB (4.5 nS) (81), and CpnT (1.36 nS) (82) or nonmycobacterial porins such as OmpA (50 to 320 pS) (83), OmpC/F (0.47/0.84 nS) (84), OmpG (0.8 nS) (85), or HiB (0.85 nS) (86). An important point to note is that we do not know if the channel conductance of refolded PPE64 is fully representative of native PPE64. However, the fact that we specifically observe channel activity only from fraction 14 of OPOE refolded PPE64 suggests that the protein is in a folded state that supports channel formation in a lipid bilayer. Altogether, our observations support an emerging theme that mycobacterial PPE proteins can function as channel proteins in the mycomembrane for the transport of different molecules. We hypothesize that the drastically different mycomembrane architecture (87) has directed *Mtb* evolution to use PPE proteins as channel proteins. Some PPE proteins have a cognate PE (proline-glutamate motif) protein partner (18, 19), and these *ppe-pe* genes are often in tandem in the chromosome. However, not all PPE proteins have or even need an interacting PE partner. Our lipid bilayer experiments show that PPE64 is in a folded state that supports channel formation without requiring a PE partner. To date, crystal structures of only smaller PPE proteins with a PE protein partner have been resolved (60, 88), leaving a huge gap in our knowledge of how channel-forming PPE proteins function. Since mycobacterial PPE proteins are primarily found in pathogenic mycobacteria, understanding their mechanisms in nutrient acquisition, particularly in iron acquisition, makes them prime candidates for developing highly targeted chemotherapy. In conclusion, we believe our study presents exciting new findings that will open new avenues in mycobacterial research.

MATERIALS AND METHODS

Bacterial strains, growth media, and molecules. Wild-type *Mycobacterium tuberculosis* H37Rv and its derivative strains were grown in Middlebrook liquid 7H9 or solid 7H10 medium supplemented with 10% ADS (8.5 g/L NaCl, 20 g/L dextrose, and 50 g/L bovine albumin fraction V), 0.5% glycerol, 0.2% Casamino Acids (CAA), and 0.02% tyloxapol. This fully supplemented medium is referred to as complete 7H9 medium from hereon. *Escherichia coli* DH5 α was grown in either LB medium containing appropriate antibiotics at 37°C with shaking at 200 rpm. The following antibiotics were used when required: ampicillin (Amp) at 100 μ g/mL for *E. coli*, kanamycin (Kan) at 30 μ g/mL for mycobacteria and 50 μ g/mL for *E. coli*, hygromycin (Hyg) at 200 μ g/mL for *E. coli*, and 50 μ g/mL for mycobacteria.

Preparation of iron-free medium. 7H9 is a defined medium whose composition is known and by default contains 150 μ M ferric citrate. All components except ferric citrate were dissolved in millipore water in acid-washed beakers to prepare the base iron-free 7H9 medium (7H9_{-Fe}). Lyophilized albumin was added to this base medium to prepare the base iron-free albumin-7H9 medium (7H9A_{-Fe}). The

medium was then filter sterilized through a 0.2- μ m filter. Freshly made ferric citrate or hemin solution was added to either base medium to prepare the specific iron-containing medium. Hemin solutions were prepared in Tris buffer as described previously (35). 2,2-Dipyridyl (DIP) iron chelator solutions were prepared in DMSO and added to freshly made hemin medium.

Growth experiments for determining iron utilization. Unless specified, all liquid cultures were grown in sealed square PETG bottles with shaking at 120 rpm, all incubation was done at 37°C, and all liquid and solid growth medium experiments were performed in triplicate. Strains were first grown to the midexponential phase in complete 7H9, then washed in sterile PBS containing tyloxapol, and then iron depleted for 10 generations in iron-free 7H9 medium containing ADS, glycerol, CAA, and tyloxapol. This iron-depletion protocol was strictly performed before all growth experiments. Iron-depleted cells were passed through a 5.0- μ m filter to obtain a single cell suspension, which was then used to inoculate iron-free liquid 7H9 or plate on iron-free solid 7H10 agar containing specific iron sources as mentioned in the main text. For plating on solid agar plates (Fig. 5E and F; Fig. S1F to H), single cell suspension was prepared at OD₆₀₀ 0.05, which was serially diluted, and 5 μ L of each dilution was spotted on agar plates. Solid agar medium was grown for 35 to 50 days as described in the figure legends. Bovine serum albumin was added to the medium to a final concentration of 0.5% wt/vol (75 μ M) for albumin growth experiments. Unless specified, all heme media (liquid and solid) in our study contained 50 μ M the iron chelator 2,2-dipyridyl (DIP). For growth experiments in Fig. 2B and C, strains were inoculated in 30 mL of medium at an initial optical density of OD₆₀₀ 0.01. For growth experiments in Fig. 2D, strains were inoculated in a final volume of 200 μ L in 96-well plates at an initial optical density of OD₆₀₀ 0.001 in wells containing various concentrations of heme. The growth of strains was determined by measuring endpoint OD₆₀₀ on days 21 and 35. For growth experiments in Fig. 5A to D, strains were inoculated in a final volume of 200 μ L in 96 wells plates at an initial optical density of OD₆₀₀ 0.001 in wells containing various concentrations of ferric citrate or heme. The growth of strains was determined by measuring endpoint OD₆₀₀ on day 18 for ferric citrate and day 30 for heme. The optical density of liquid cultures was measured using a BioTek Synergy plate reader. All experiments were performed with a minimum of three biological replicates.

Ethidium bromide accumulation assay. Strains were first grown to log phase in 30 mL of complete 7H9 medium and then filtered through a 5.0- μ m filter to obtain a single-cell suspension. Cells were then harvested by low-speed centrifugation at 1,500 \times g for 10 min and resuspended to a final OD₆₀₀ of 1.0 in uptake buffer (76 mM (NH₄)₂SO₄, 0.5 M KH₂PO₄, 1 mM MgSO₄, 0.4% glucose, and 0.05% Tween 80). For both strains, 100 μ L of cells was added in triplicate in a 96-well plate and ethidium bromide was then added to a final concentration of 20 μ M. Fluorescence was measured by excitation at 530 nm and emission at 590 nm at 1 min intervals for 20 min.

Transcriptomic analysis, RNA extraction, and real-time PCR. Iron-depleted wt *Mtb* was inoculated in triplicates into 60 mL of albumin-free iron-free 7H9 containing either 10 μ M FeCi or 10 μ M heme at an initial optical density of OD₆₀₀ 0.01. Strains were grown to the midexponential phase to OD₆₀₀ ~1.0. Total RNA was extracted exactly as we did previously (8) and mRNA was isolated using NEBNext rRNA Depletion kit (E7850L). RNA sequencing and bioinformatic analysis were performed at the Microbial Pathogenesis and Genomics Core Center at the University of Oklahoma Health Science Center. Sequence reads were aligned to *Mtb* H37Rv genome (NC_000962). Differential expression analysis was performed with DESeq (21) comparing the heme growth condition to the standard FeCi condition. Three hundred seventeen out of 3,968 genes (8.5%) with nonzero read counts were differentially expressed at least 2-fold with a false discovery rate (FDR) adjusted $P < 0.01$ (181 up in heme, 135 down). To compare expression levels of genes between wt and Δ *sigM*, iron-depleted strains were inoculated at OD₆₀₀ of 1.0 in triplicates into 60 mL of albumin-free iron-free 7H9 containing 10 μ M heme and incubated for 48 h. Cells were harvested, and total RNA was extracted. cDNA synthesis was performed using the Bio-Rad iScript cDNA Synthesis kit as per the manufacturer's protocol. qRT-PCR cycling conditions for relative quantitation of gene expression were performed using Realplex EP Gradient S Real-Time cyler (Eppendorf). Cycle threshold (C_t) data were normalized to *rrs* (*Mtb* 16S rRNA gene), and normalized C_t values (Δ C_t) were transformed to arbitrary gene expression units using the 2^{- Δ C_t}/10⁻⁶ method as described by Livak and Schmittgen (36).

Targeted gene deletion in *Mtb*. To construct mutants, 1,000 bp of left (L) and 1,000 bp right (R) flanking sequences of the target gene were amplified using corresponding primer pairs LF/Spel-LR/Swal and RF/Pacl-RR/Nsil (Table S3), respectively, and cloned into pML2424 to construct gene deletion vectors (Table S3). The deletion vectors were then transformed into *Mtb*. Transformants were selected at 37°C on 7H10 Hyg and visually validated through the presence of both GFP and RFP fluorescence. Liquid culture of the transformant was then plated on 7H10 Hyg containing 2% sucrose at 40°C for the selection of double crossovers. Putative double crossovers were visually analyzed for the presence of only GFP, and gene deletion was validated by PCR. For excision of the *loxP*-flanked *gfp*²⁺_m-*hyg* cassette, pML2714 expressing Cre recombinase was transformed into marked mutants and unmarked mutants were selected on 7H10 Kan at 37°C. Putative unmarked mutants were first visually validated through the absence of GFP fluorescence and then through PCR (Fig. S1; Fig. S3) (validation primers [V/F-V/R], Table S3) and loss of growth on hygromycin. All validated mutants were designated an OALnumber (Table S3) for identification.

Construction of mycobacterial expression and protein purification vectors. All primers and vectors are described in Table S3. The orf of *eccC4* was cloned into pML1335 vector using corresponding primers to generate the *eccC4* integrative expression vector pOAL102. The ORF of *hs1-M7A* was cloned into pMN016 using corresponding primers to generate the episomal heme sensor expression vector pOAL311. C-terminally HA-tagged integrative expression vectors for *ppe36* (pOAL313), *ppe62* (pOAL314), and *ppe64* (pOAL317) were generated by cloning ORFs into pML1335 using corresponding primers.

Integrative expression vectors for *rv0125* (pOAL319), *rv1085c* (pOAL320), and *sigM* (pOAL321) were generated by cloning ORFs into pML2300 using corresponding primers. All mycobacterial expression vectors use the strong *psymc* promoter for gene expression. All vectors used for protein purification were constructed by cloning ORFs into pET21a+ using corresponding primers.

Temporal analysis of heme biosensors. Transformants of pOAL311 (HS1-M7A) in wt and $\Delta eccC4$ were selected on 7H10 Hyg agar plates. Iron-depleted strains were inoculated at OD₆₀₀ of 1.0 in triplicates into 10 mL of albumin-free iron-free 7H9 containing either 10 μ M FeCl₃ or 10 μ M heme. Cells were grown in the specific medium, and fluorescence for each biosensor was measured at the specific time points as mentioned in the text (Fig. 3). eGFP fluorescence was measured by excitation/emission at 480 nm/510 nm, and mKATE2 fluorescence was measured by excitation/emission at 580 nm/620 nm. HS1-M7A fluorescence is reported as a ratio of eGFP/mKATE2. For determining biosensor functionality (Fig. 3A), the wt transformant was inoculated in the medium at an initial optical density of OD₆₀₀ 0.01. For comparing biosensor fluorescence between wt and $\Delta eccC4$ (Fig. 3B), strains were inoculated at a high initial optical density of OD₆₀₀ 1.0 because the *eccC4* strain has a significant growth delay in heme and so that enough cells were available for fluorescence measurements. Optical density and fluorescence were measured using a BioTek Synergy plate reader.

Subcellular fractionation and surface accessibility assays. All experiments were performed as we did previously (9). Iron-depleted cells (Table S3) were grown in 120 mL of 7H9C with Hyg to an OD₆₀₀ of 2. Cells were lysed by sonication and soluble and membrane fractions were separated by ultracentrifugation at 100,000 $\times g$ for 1 h at 4°C. The supernatant (C1) was transferred to a separate tube, and the pellet was resuspended in the same volume of PBS as C1 and designated M1. Both C1 and M1 fractions were centrifuged at 100,000 $\times g$ for 1 h at 4°C. The supernatant containing the cytosolic fraction was transferred to a new tube and labeled C2, and the membrane pellet fraction was resuspended in the same volume of PBS as that used for C2 and designated M2. HA-tagged proteins in L, M2, and C2 fractions were detected in Western blots using primary mouse anti-HA (Invitrogen; MA527543) antibody. Primary monoclonal mouse antibodies were used for detecting LpqH (BEI; NR-50098) and RNA polymerase (Invitrogen; MA125425). Secondary horseradish peroxidase-conjugated goat anti-mouse (Bio-Rad; 1706516) antibody was in all blots, which were developed using ECL substrate (Bio-Rad; 1705061), and luminescence was visualized using Bio-Rad Chemidoc MP imaging system. Strains expressing HA-tagged proteins were grown to mid-log phase and fixed with 4% paraformaldehyde for 30 min at room temperature. The cells were washed twice with PBS-Tyloxapol (0.02%) and incubated with monoclonal rabbit anti-HA antibody at a 1:1 dilution for 2 h for bacterial surface staining. The cells were then washed three times with PBS-Tyloxapol and then stained with fluorescein isothiocyanate (FITC)-labeled anti-rabbit antibodies at a dilution of 1:100 for 2 h. The cells were again washed three times with PBS-Tyloxapol and analyzed via flow cytometry. Surface-accessible proteins were quantified by measuring fluorescence and displayed as histograms.

Harvesting culture filtrate and proteomic analysis. Iron-depleted *Mtb* and $\Delta eccC4$ were inoculated in five replicates into 30 mL of albumin-free iron-free 7H9 containing either 10 μ M FeCl₃ or 10 μ M heme at a high initial optical density of OD₆₀₀ 1.0 to ensure enough cells for appropriate comparison of protein levels. FeCl₃ culture supernatants were harvested after 8 days when both strains exhibit exponential growth (Fig. 2C). Heme culture supernatant for both strains was harvested after 20 days when wt is in exponential phase and $\Delta eccC4$ is still in lag phase (Fig. 2D). OD₆₀₀ of wt and $\Delta eccC4$ heme cultures were ~ 4.3 and ~ 1.6 , respectively. Culture supernatant was harvested by centrifugation at 5,000 $\times g$ for 10 min and then filtered through a 0.2- μ m filter. Amicon 3-kDa centrifugal filtration units were thoroughly washed with millipore water, and the filtered supernatant was concentrated >60 -fold.

Fifty micrograms of protein samples was digested using the S-trap protocol, as described by the manufacturer (37). For this, samples were adjusted to contain 5% SDS, 5 mM Tris(2-carboxyethyl)phosphine, 50 mM triethylammonium bicarbonate (TEAB), pH 8.5, and the samples were incubated for 30 min at room temperature (RT). Samples were then alkylated by adding iodoacetamide to 10 mM and incubating for 20 min at RT. The alkylated samples were then acidified by adding phosphoric acid to a 1.2% final concentration (C₁) and diluted further by adding 6 volumes of buffered methanol (90% methanol; 100 mM TEAB, pH 7.1). Samples were centrifuged through the S-trap spin filtration devices (Protifi number C02-micro), and the retentates were washed further with buffered methanol. To each washed retentate, 25 μ L of 50 mM triethylammonium bicarbonate pH 8.5 containing 0.8 μ g of trypsin/LysC (Promega) was applied, and the digestions were incubated overnight at 37°C. After digestion, peptides were collected via three successive 40- μ L elutions first using 40 mM TEAB pH 8.5, then 0.1% aqueous formic acid, and then 50:50:0.1 acetonitrile/water/formic acid, after which the pooled peptide eluates were dried by vacuum centrifugation. Peptides were analyzed by liquid chromatography-tandem mass spectrometry (LC-MS/MS) on a quadrupole-Orbitrap mass spectrometer (Fusion model, Thermo), using a "high/low" data-dependent MS/MS acquisition method. For these analyses, peptides were dissolved in mobile phase A (0.1% aqueous formic acid), and a vented trap configuration was used for injection onto a 75- μ m \times 50-cm analytical column packed with 2- μ m C18 particles (Acclaim PepMap RSLC, number 20330952, Thermo). The column was developed using 80:20:0.1 acetonitrile/water/formic acid as mobile phase B, transitioning linearly from 4% mobile phase B to 32% mobile phase B over a period of 120 min at a uniform 250 nL/min flow rate. Eluting peptides were ionized in a Nanospray Flex ion source (Thermo) using a stainless-steel emitter. Peptide ions were analyzed in the Orbitrap sector at a nominal resolution of 120,000, selected for MS/MS using the quadrupole sector, fragmented by higher-energy collisional dissociation in the ion routing multipole sector, and the fragment ions analyzed in the ion trap sector. The specific instrument settings are provided in Table S2 and are also available through the PRIDE data archive (project [PXD036081](https://www.ebi.ac.uk/pride/projects/PXD036081)).

To identify and quantify peptides and infer protein abundances, MaxQuant v2.0.1.0 (89) was used to

analyze the raw instrument files. The reference proteome of 3,993 *M. tuberculosis* H37Rv sequences was downloaded from Uniprot. Searches utilized default settings in MaxQuant, supplemented with the variable modification cyclization of glutamine to pyroglutamate, with the Match Between Runs enabled, and with LFQ and iBAQ quantifications enabled (90). The label-free quantification (LFQ) values of 2,615 proteins (Table S2) were further used to compare proteomes. Reversed decoy proteins identifications and contaminants were filtered out and protein intensities were \log_2 transformed. Data were normalized by subtracting the median. SAM analysis (38) was performed using the volcano plot tool in Perseus (91) using a permutation-corrected FDR of 5% to control for multiple hypotheses testing one-way and an S0 value of 0.1.

Isolation of inclusion bodies, protein purification, and protein refolding. Transformants of pOAL301, pOAL306, and pOAL312 in *E. coli* BL21(DE3) were selected on LB Amp agar plates. All proteins were purified using the same method. Briefly, starter cultures of strains were inoculated into 500 mL of fresh LB medium with ampicillin and grown to an OD_{600} of 0.3. Gene expression was induced with 1 mM IPTG at 18°C for 18 h. After induction of gene expression *E. coli*, cells were harvested by centrifugation and lysed by sonication in ice-cold base buffer (BB; 50 mM NaPi, 150 mM NaCl, pH 7.4). The cell lysate was clarified by low-speed centrifugation at $1,500 \times g$, 4°C for 10 min, and the supernatant containing whole-cell lysate (Fig. 7A, lane 1) was removed to a fresh tube. To solubilize all membrane proteins, Triton X-100 was added to the lysate at 1% C_r and incubated on ice for 20 min. The lysate was then centrifuged at $15,000 \times g$, 4°C for 15 min, and the supernatant (Fig. 7A, lane 2) was removed leaving the inclusion bodies (IB) in the pellet. The IB pellet was washed twice with BB (Fig. 7A, lanes 3 to 4) and then solubilized with BB containing 8 M Urea (BBU) (Fig. 7A, lane 5). Solubilized IB was loaded on to activated nickel resin and bound at room temperature for 2 h. Flow through was collected (Fig. 7A, lane 6), and protein-loaded resin was washed twice with BBU containing 40 mM imidazole (Fig. 7A, lanes 7 to 8) wash buffer. The target protein was eluted with BBU containing 500 mM imidazole (Fig. 7A, lanes 9 to 15). The cleanest elutions as visualized through gel electrophoresis were used for subsequent dialysis and refolding of protein. OPOE or DDM detergent was added to eluted protein to 0.5% or 0.1% C_r , respectively. Dialysis buffer (DB) was prepared by adding OPOE or DDM to BB to 0.5% or 0.1% C_r , respectively. A protein sample (1 mL) was loaded into a Thermo Slide-A-Lyzer 3.5-kDa dialysis cassette, and urea was removed by dialysis with 400 mL of DB. DB was replaced at 24 h, and dialysis was performed for a total of 48 h at 4°C with low spin. PPE36, MhuD, and IdeR were all purified as we did previously (9). MspA was selectively purified by heat extraction as described previously (42). Briefly, a 50-mL culture of *M. smegmatis* mc²155 was first grown in 7H9 medium to the midexponential phase. Cells were harvested by centrifugation at $5,000 \times g$ for 5 min, washed three times with PBS, and then resuspended in 0.3 mL of PG05 buffer (0.5% Genapol, 100 mM Na_2HPO_4/NaH_2PO_4 , 0.1 mM EDTA, and 150 mM NaCl, pH 6.5). Protein was first extracted by incubating cells for 30 min at 100°C, the sample was then cooled on ice and centrifuged to remove debris, and the supernatant containing MspA was used for SDS-PAGE and bilayer analysis.

Absorption and surface plasmon resonance spectroscopy for detecting heme binding. Fresh solutions of heme in were prepared in Tris buffer. An equimolar amount of heme was added to 10 μ M protein and incubated a room temperature for 5 min. For difference absorption spectroscopy, heme binding was monitored using a Bio-Tek Synergy HT plate reader by subtracting the free heme spectra from the protein incubated heme spectra. Surface plasmon resonance (SPR) experiments were performed at University of Alabama at Birmingham SPR core facility exactly as we did before (9).

Lipid bilayer experiments, recording, and data analysis. Bilayer experiments were performed using very similar instrumentation and methods as described by Zakharian and Reusch (92). Synthetic diphytanoyl phosphatidylcholine (DphPC; Avanti Polar Lipids, Birmingham, AL) was used to form planar lipid bilayers. Lipids were solubilized in *n*-Decane at 20 mg/mL, and a glass capillary tube was used to paint a bilayer in an aperture of 200 μ m diameter in a Delrin cup (Warner Instruments, Hamden, CT). The bilayer was painted between an aqueous solution of 1 M KCl, 10 mM HEPES, pH 7.1, and capacitance was registered in the range of 66 to 100 pF. Approximately ~40 ng of purified OPOE refolded protein in 1 to 2 μ L volume was added to the *cis* compartment and channel-forming activity was recorded at 30-mV applied potential. The current trace was recorded with a patch-clamp amplifier (BC-535 Bilayer Clamp, Warner Instruments). The *trans* and *cis* solutions were connected to the head stage point with Ag-AgCl electrodes. Currents were low-pass filtered at 10 kHz and then digitized through an analog-to-digital converter (Digidata 1550B; Molecular Devices, San Jose, CA). Data filtering was done at 100 Hz through an 8-pole Bessel Filter (Lpf-8; Warner Instruments) and digitized at 1 kHz using pClamp11 software (Molecular Devices). Single-channel conductance events were identified automatically using Clampfit11 from 5 independent membrane recordings.

Data availability. All source data files are provided and/or publicly available and are also available to anyone upon request. RNAseq data files are available through the NCBI Sequence Read Archive (BioProject ID [PRJNA868362](https://www.ncbi.nlm.nih.gov/bioproject/PRJNA868362)). Mass spectrometry data files are available through the PRIDE Data Archive ([PXD036081](https://www.ebi.ac.uk/pride/archive/projects/PXD036081)). Lipid bilayer data acquisition files (axon binary file) require pClamp software, which to the best of our knowledge is only available for purchase through Molecular Devices. All requests should be addressed to Avishek Mitra.

SUPPLEMENTAL MATERIAL

Supplemental material is available online only.

FIG S1, TIF file, 2.6 MB.

FIG S2, TIF file, 1.5 MB.

FIG S3, TIF file, 2.4 MB.

FIG S4, TIF file, 2.8 MB.

FIG S5, TIF file, 3.6 MB.

FIG S6, TIF file, 1.3 MB.

TABLE S1, XLSX file, 0.8 MB.

TABLE S2, XLSX file, 0.8 MB.

TABLE S3, DOCX file, 0.04 MB.

ACKNOWLEDGMENTS

We thank Michael Niederweis for sharing parent vectors for use in this study. We thank the University of Alabama at Birmingham SPR core facility for assistance with the SPR experiments. We thank the Laboratory for Molecular Biology and Cytometry Research at OUHSC for the use of the Core Facility which provided RNA sequencing and bioinformatics service.

This study was supported in part by NIH grant P20GM134973, an NIH-funded program that was made possible by NIGMS, and Oklahoma State University College of Arts and Sciences startup funds awarded to A.M.

A.M. conceived the project; N.S. and H.M. contributed equally to the project; A.M. and S.H. directed research; N.S., H.M., J.R., A.R., S.D.H., and A.M. designed experiments and analyzed data; N.S., H.M., P.S., and J.R. performed research; N.S., H.M., S.D.H., and A.M. wrote and edited the manuscript.

The authors declare no competing interests.

REFERENCES

- World Health Organization. 2021. Global tuberculosis report 2021. World Health Organization, Geneva, Switzerland.
- Skaar EP. 2010. The battle for iron between bacterial pathogens and their vertebrate hosts. *PLoS Pathog* 6:e1000949. <https://doi.org/10.1371/journal.ppat.1000949>.
- Cassat JE, Skaar EP. 2013. Iron in infection and immunity. *Cell Host Microbe* 13:509–519. <https://doi.org/10.1016/j.chom.2013.04.010>.
- Skaar EP, Raffatellu M. 2015. Metals in infectious diseases and nutritional immunity. *Metallomics* 7:926–928. <https://doi.org/10.1039/c5mt90021b>.
- White AJ, Snow GA. 1969. Isolation of mycobactins from various mycobacteria. The properties of mycobactin S and H. *Biochem J* 111:785–792. <https://doi.org/10.1042/bj1110785>.
- Snow GA. 1969. Metal complexes of mycobactin P and of desferriseridamines. *Biochem J* 115:199–205. <https://doi.org/10.1042/bj1150199>.
- Runyen-Janecky LJ. 2013. Role and regulation of heme iron acquisition in gram-negative pathogens. *Front Cell Infect Microbiol* 3:55. <https://doi.org/10.3389/fcimb.2013.00055>.
- Mitra A, Ko YH, Cingolani G, Niederweis M. 2019. Heme and hemoglobin utilization by *Mycobacterium tuberculosis*. *Nat Commun* 10:4260. <https://doi.org/10.1038/s41467-019-12109-5>.
- Mitra A, Speer A, Lin K, Ehrt S, Niederweis M. 2017. PPE surface proteins are required for heme utilization by *Mycobacterium tuberculosis*. *mBio* 8:e01720-16. <https://doi.org/10.1128/mBio.01720-16>.
- Jones CM, Niederweis M. 2011. *Mycobacterium tuberculosis* can utilize heme as an iron source. *J Bacteriol* 193:1767–1770. <https://doi.org/10.1128/JB.01312-10>.
- Tullius MV, Harmston CA, Owens CP, Chim N, Morse RP, McMath LM, Iniguez A, Kimmey JM, Sawaya MR, Whitelegge JP, Horwitz MA, Goulding CW. 2011. Discovery and characterization of a unique mycobacterial heme acquisition system. *Proc Natl Acad Sci U S A* 108:5051–5056. <https://doi.org/10.1073/pnas.1009516108>.
- Huang W, Wilks A. 2017. Extracellular heme uptake and the challenge of bacterial cell membranes. *Annu Rev Biochem* 86:799–823. <https://doi.org/10.1146/annurev-biochem-060815-014214>.
- Tullius MV, Nava S, Horwitz MA. 2019. PPE37 is essential for mycobacterium tuberculosis heme-iron acquisition (HIA), and a defective PPE37 in *Mycobacterium bovis* BCG prevents HIA. *Infect Immun* 87:e00540-18. <https://doi.org/10.1128/IAI.00540-18>.
- Adams PA, Berman MC. 1980. Kinetics and mechanism of the interaction between human serum albumin and monomeric haemin. *Biochem J* 191:95–102. <https://doi.org/10.1042/bj1910095>.
- Pinsky M, Roy U, Moshe S, Weissman Z, Kornitzer D. 2020. Human serum albumin facilitates heme-iron utilization by fungi. *mBio* 11:e00607-20. <https://doi.org/10.1128/mBio.00607-20>.
- Groschel MI, Sayes F, Simeone R, Majlessi L, Brosch R. 2016. ESX secretion systems: mycobacterial evolution to counter host immunity. *Nat Rev Microbiol* 14:677–691. <https://doi.org/10.1038/nrmicro.2016.131>.
- Vaziri F, Brosch R. 2019. ESX/Type VII secretion systems—an important way out for mycobacterial proteins. *Microbiol Spectr* 7:7.4.10. <https://doi.org/10.1128/microbiolspec.PSIB-0029-2019>.
- Fishbein S, van Wyk N, Warren RM, Sampson SL. 2015. Phylogeny to function: PE/PPE protein evolution and impact on *Mycobacterium tuberculosis* pathogenicity. *Mol Microbiol* 96:901–916. <https://doi.org/10.1111/mmi.12981>.
- Sampson SL. 2011. Mycobacterial PE/PPE proteins at the host-pathogen interface. *Clin Dev Immunol* 2011:497203. <https://doi.org/10.1155/2011/497203>.
- Rodriguez GM, Voskuil MI, Gold B, Schoolnik GK, Smith I. 2002. *ideR*, An essential gene in *Mycobacterium tuberculosis*: role of *IdeR* in iron-dependent gene expression, iron metabolism, and oxidative stress response. *Infect Immun* 70:3371–3381. <https://doi.org/10.1128/IAI.70.7.3371-3381.2002>.
- Anders S, Huber W. 2010. Differential expression analysis for sequence count data. *Genome Biol* 11:R106. <https://doi.org/10.1186/gb-2010-11-10-r106>.
- Quadri LE, Sello J, Keating TA, Weinreb PH, Walsh CT. 1998. Identification of a *Mycobacterium tuberculosis* gene cluster encoding the biosynthetic enzymes for assembly of the virulence-conferring siderophore mycobactin. *Chem Biol* 5:631–645. [https://doi.org/10.1016/s1074-5521\(98\)90291-5](https://doi.org/10.1016/s1074-5521(98)90291-5).
- Jones CM, Wells RM, Madduri AV, Renfrow MB, Ratledge C, Moody DB, Niederweis M. 2014. Self-poisoning of *Mycobacterium tuberculosis* by interrupting siderophore recycling. *Proc Natl Acad Sci U S A* 111:1945–1950. <https://doi.org/10.1073/pnas.1311402111>.
- Wells RM, Jones CM, Xi Z, Speer A, Danilchanka O, Doornbos KS, Sun P, Wu F, Tian C, Niederweis M. 2013. Discovery of a siderophore export system essential for virulence of *Mycobacterium tuberculosis*. *PLoS Pathog* 9:e1003120. <https://doi.org/10.1371/journal.ppat.1003120>.
- Arnold FM, Weber MS, Gonda I, Gallenito MJ, Adenau S, Egloff P, Zimmermann I, Hutter CAJ, Hurlimann LM, Peters EE, Piel J, Meloni G, Medalia O, Seeger MA. 2020. The ABC exporter *IrtAB* imports and reduces mycobacterial siderophores. *Nature* 580:413–417. <https://doi.org/10.1038/s41586-020-2136-9>.
- Ryndak MB, Wang S, Smith I, Rodriguez GM. 2010. The *Mycobacterium tuberculosis* high-affinity iron importer, *IrtA*, contains an FAD-binding domain. *J Bacteriol* 192:861–869. <https://doi.org/10.1128/JB.00223-09>.

27. Rodriguez GM, Smith I. 2006. Identification of an ABC transporter required for iron acquisition and virulence in *Mycobacterium tuberculosis*. *J Bacteriol* 188:424–430. <https://doi.org/10.1128/JB.188.2.424-430.2006>.
28. Hanna DA, Martinez-Guzman O, Reddi AR. 2017. Heme gazing: illuminating eukaryotic heme trafficking, dynamics, and signaling with fluorescent heme sensors. *Biochemistry* 56:1815–1823. <https://doi.org/10.1021/acs.biochem.7b00007>.
29. Hanna DA, Harvey RM, Martinez-Guzman O, Yuan X, Chandrasekharan B, Raju G, Outten FW, Hamza I, Reddi AR. 2016. Heme dynamics and trafficking factors revealed by genetically encoded fluorescent heme sensors. *Proc Natl Acad Sci U S A* 113:7539–7544. <https://doi.org/10.1073/pnas.1523802113>.
30. Donegan RK, Fu Y, Copeland J, Idga S, Brown G, Hale OF, Mitra A, Yang H, Dailey HA, Niederweis M, Jain P, Reddi AR. 2022. Exogenously scavenged and endogenously synthesized heme are differentially utilized by *Mycobacterium tuberculosis*. *Microbiol Spectr* 10:e0360422. <https://doi.org/10.1128/spectrum.03604-22>.
31. Kaps I, Eht S, Seeber S, Schnappinger D, Martin C, Riley LW, Niederweis M. 2001. Energy transfer between fluorescent proteins using a co-expression system in *Mycobacterium smegmatis*. *Gene* 278:115–124. [https://doi.org/10.1016/s0378-1119\(01\)00712-0](https://doi.org/10.1016/s0378-1119(01)00712-0).
32. Kapopoulou A, Lew JM, Cole ST. 2011. The MycoBrowser portal: a comprehensive and manually annotated resource for mycobacterial genomes. *Tuberculosis (Edinb)* 91:8–13. <https://doi.org/10.1016/j.tube.2010.09.006>.
33. Arraiz N, Salazar L, Lopez G, Rodriguez R, Casart Y, Takiff H. 2001. Characterization of the expression and function of SigM an ECF sigma factor in mycobacteria. *Acta Cient Venez* 52(Suppl 1):40–41.
34. Clark RR, Judd J, Lasek-Nesselquist E, Montgomery SA, Hoffmann JG, Derbyshire KM, Gray TA. 2018. Direct cell-cell contact activates SigM to express the ESX-4 secretion system in *Mycobacterium smegmatis*. *Proc Natl Acad Sci U S A* 115:E6595–E6603. <https://doi.org/10.1073/pnas.1804227115>.
35. Chim N, Iniguez A, Nguyen TQ, Goulding CW. 2010. Unusual diheme conformation of the heme-degrading protein from *Mycobacterium tuberculosis*. *J Mol Biol* 395:595–608. <https://doi.org/10.1016/j.jmb.2009.11.025>.
36. Livak KJ, Schmittgen TD. 2001. Analysis of relative gene expression data using real-time quantitative PCR and the 2(-delta delta C(T)) method. *Methods* 25:402–408. <https://doi.org/10.1006/meth.2001.1262>.
37. HaileMariam M, Eguez RV, Singh H, Bekele S, Ameni G, Pieper R, Yu Y. 2018. S-Trap, an Ultrafast sample-preparation approach for shotgun proteomics. *J Proteome Res* 17:2917–2924. <https://doi.org/10.1021/acs.jproteome.8b00505>.
38. Tusher VG, Tibshirani R, Chu G. 2001. Significance analysis of microarrays applied to the ionizing radiation response. *Proc Natl Acad Sci U S A* 98:5116–5121. <https://doi.org/10.1073/pnas.091062498>.
39. Korycka-Machala M, Pawelczyk J, Borowska P, Dziadek B, Brzostek A, Kawka M, Bekier A, Rykowski S, Olejniczak AB, Strapagiel D, Witczak Z, Dziadek J. 2020. PPE51 is involved in the uptake of disaccharides by *Mycobacterium tuberculosis*. *Cells* 9:603. <https://doi.org/10.3390/cells9030603>.
40. Wang Q, Boshoff HIM, Harrison JR, Ray PC, Green SR, Wyatt PG, Barry CE, III. 2020. PE/PPE proteins mediate nutrient transport across the outer membrane of *Mycobacterium tuberculosis*. *Science* 367:1147–1151. <https://doi.org/10.1126/science.aav5912>.
41. Faller M, Niederweis M, Schulz GE. 2004. The structure of a mycobacterial outer-membrane channel. *Science* 303:1189–1192. <https://doi.org/10.1126/science.1094114>.
42. Heinz C, Niederweis M. 2000. Selective extraction and purification of a mycobacterial outer membrane protein. *Anal Biochem* 285:113–120. <https://doi.org/10.1006/abio.2000.4728>.
43. Pavlenok M, Niederweis M. 2016. Hetero-oligomeric MspA pores in *Mycobacterium smegmatis*. *FEMS Microbiol Lett* 363:fnw046 <https://doi.org/10.1093/femsle/fnw046>.
44. Gray TA, Clark RR, Boucher N, Lapierre P, Smith C, Derbyshire KM. 2016. Inter-cellular communication and conjugation are mediated by ESX secretion systems in mycobacteria. *Science* 354:347–350. <https://doi.org/10.1126/science.aag0828>.
45. Laencina L, Dubois V, Le Moigne V, Viljoen A, Majlessi L, Pritchard J, Bernut A, Piel L, Roux AL, Gaillard JL, Lombard B, Loew D, Rubin EJ, Brosch R, Kremer L, Herrmann JL, Girard-Misguich F. 2018. Identification of genes required for *Mycobacterium abscessus* growth in vivo with a prominent role of the ESX-4 locus. *Proc Natl Acad Sci U S A* 115:E1002–E1011. <https://doi.org/10.1073/pnas.1713195115>.
46. Izquierdo Lafuente B, Ummels R, Kuijl C, Bitter W, Speer A. 2021. *Mycobacterium tuberculosis* toxin CpnT Is an ESX-5 substrate and requires three type VII secretion systems for intracellular secretion. *mBio* 12:e02983-20. <https://doi.org/10.1128/mBio.02983-20>.
47. Wang Y, Tang Y, Lin C, Zhang J, Mai J, Jiang J, Gao X, Li Y, Zhao G, Zhang L, Liu J. 2022. Crosstalk between the ancestral type VII secretion system ESX-4 and other T7SS in *Mycobacterium marinum*. *iScience* 25:103585. <https://doi.org/10.1016/j.isci.2021.103585>.
48. Pajuelo D, Tak U, Zhang L, Danilchanka O, Tischler AD, Niederweis M. 2021. Toxin secretion and trafficking by *Mycobacterium tuberculosis*. *Nat Commun* 12:6592. <https://doi.org/10.1038/s41467-021-26925-1>.
49. Siegrist MS, Steigedal M, Ahmad R, Mehra A, Dragset MS, Schuster BM, Philips JA, Carr SA, Rubin EJ. 2014. Mycobacterial Esx-3 requires multiple components for iron acquisition. *mBio* 5:e01073-14–e01014. <https://doi.org/10.1128/mBio.01073-14>.
50. Serafini A, Pisu D, Palu G, Rodriguez GM, Manganelli R. 2013. The ESX-3 secretion system is necessary for iron and zinc homeostasis in *Mycobacterium tuberculosis*. *PLoS One* 8:e78351. <https://doi.org/10.1371/journal.pone.0078351>.
51. Serafini A, Boldrin F, Palu G, Manganelli R. 2009. Characterization of a *Mycobacterium tuberculosis* ESX-3 conditional mutant: essentiality and rescue by iron and zinc. *J Bacteriol* 191:6340–6344. <https://doi.org/10.1128/JB.00756-09>.
52. Siegrist MS, Unnikrishnan M, McConnell MJ, Borowsky M, Cheng TY, Siddiqi N, Fortune SM, Moody DB, Rubin EJ. 2009. Mycobacterial Esx-3 is required for mycobactin-mediated iron acquisition. *Proc Natl Acad Sci U S A* 106:18792–18797. <https://doi.org/10.1073/pnas.0900589106>.
53. Kurthkoti K, Amin H, Marakalala MJ, Ghanny S, Subbian S, Sakatos A, Livny J, Fortune SM, Berney M, Rodriguez GM. 2017. The capacity of mycobacterium tuberculosis to survive iron starvation might enable it to persist in iron-deprived microenvironments of human granulomas. *mBio* 8:e01092-17. <https://doi.org/10.1128/mBio.01092-17>.
54. Rivera-Calzada A, Famelis N, Llorca O, Geibel S. 2021. Type VII secretion systems: structure, functions and transport models. *Nat Rev Microbiol* 19:567–584. <https://doi.org/10.1038/s41579-021-00560-5>.
55. Daleke MH, Ummels R, Bawono P, Heringa J, Vandenbroucke-Grauls CM, Luirink J, Bitter W. 2012. General secretion signal for the mycobacterial type VII secretion pathway. *Proc Natl Acad Sci U S A* 109:11342–11347. <https://doi.org/10.1073/pnas.1119453109>.
56. Poulsen C, Panjikar S, Holton SJ, Wilmanns M, Song YH. 2014. WXG100 Protein Superfamily consists of three subfamilies and exhibits an alpha-helical C-terminal conserved residue pattern. *PLoS One* 9:e89313. <https://doi.org/10.1371/journal.pone.0089313>.
57. Agarwal N, Woolwine SC, Tyagi S, Bishai WR. 2007. Characterization of the *Mycobacterium tuberculosis* sigma factor SigM by assessment of virulence and identification of SigM-dependent genes. *Infect Immun* 75:452–461. <https://doi.org/10.1128/IAI.01395-06>.
58. Raman S, Puyang X, Cheng TY, Young DC, Moody DB, Husson RN. 2006. Mycobacterium tuberculosis SigM positively regulates Esx secreted protein and nonribosomal peptide synthetase genes and down regulates virulence-associated surface lipid synthesis. *J Bacteriol* 188:8460–8468. <https://doi.org/10.1128/JB.01212-06>.
59. Lagune M, Le Moigne V, Johansen MD, Vasquez Sotomayor F, Daher W, Petit C, Cosentino G, Paulowski L, Gutschmann T, Wilmanns M, Maurer FP, Herrmann JL, Girard-Misguich F, Kremer L. 2022. The ESX-4 substrates, EsxU and EsxT, modulate *Mycobacterium abscessus* fitness. *PLoS Pathog* 18:e1010771. <https://doi.org/10.1371/journal.ppat.1010771>.
60. Williamson ZA, Chaton CT, Ciocca WA, Korotkova N, Korotkov KV. 2020. PE5-PPE4-EspG3 heterotrimer structure from mycobacterial ESX-3 secretion system gives insight into cognate substrate recognition by ESX systems. *J Biol Chem* 295:12706–12715. <https://doi.org/10.1074/jbc.RA120.012698>.
61. Korotkova N, Freire D, Phan TH, Ummels R, Creekmore CC, Evans TJ, Wilmanns M, Bitter W, Parret AH, Houben EN, Korotkov KV. 2014. Structure of the *Mycobacterium tuberculosis* type VII secretion system chaperone EspG5 in complex with PE25-PPE41 dimer. *Mol Microbiol* 94:367–382. <https://doi.org/10.1111/mmi.12770>.
62. Newton-Foot M, Gey van Pittius NC. 2013. Understanding the evolution and function of the mycobacterial type VII ESX secretion systems (T7SSs) and their substrates. PhD dissertation. Stellenbosch University, Stellenbosch, South Africa. https://www.google.com/url?sa=t&rc=1&q=&esrc=s&source=web&cd=&cad=rja&uact=8&ved=2ahUKewiHxfYulz5AhWUImoFHUpPAMMQFnoEACaQAQ&url=https%3A%2F%2Fscholar.sun.ac.za%2Fbitstream%2Fhandle%2F10019.1%2F79805%2Fnewtonfoot_understanding_2013.pdf%3Fsequence%3D2%26isAllowed%3Dy&usq=AOvVaw17h6P-TGdrlxht4Pjkbqm.

63. Patel S. 2017. A critical review on serine protease: key immune manipulator and pathology mediator. *Allergol Immunopathol (Madr)* 45:579–591. <https://doi.org/10.1016/j.aller.2016.10.011>.
64. Otto BR, Sijbrandi R, Luirink J, Oudega B, Heddle JG, Mizutani K, Park SY, Tame JR. 2005. Crystal structure of hemoglobin protease, a heme binding autotransporter protein from pathogenic *Escherichia coli*. *J Biol Chem* 280:17339–17345. <https://doi.org/10.1074/jbc.M412885200>.
65. Otto BR, van Dooren SJ, Dozois CM, Luirink J, Oudega B. 2002. *Escherichia coli* hemoglobin protease autotransporter contributes to synergistic abscess formation and heme-dependent growth of *Bacteroides fragilis*. *Infect Immun* 70:5–10. <https://doi.org/10.1128/IAI.70.1.5-10.2002>.
66. Otto BR, van Dooren SJ, Nuijens JH, Luirink J, Oudega B. 1998. Characterization of a hemoglobin protease secreted by the pathogenic *Escherichia coli* strain EB1. *J Exp Med* 188:1091–1103. <https://doi.org/10.1084/jem.188.6.1091>.
67. Drago-Serrano ME, Parra SG, Manjarrez-Hernandez HA. 2006. EspC, an autotransporter protein secreted by enteropathogenic *Escherichia coli* (EPEC), displays protease activity on human hemoglobin. *FEMS Microbiol Lett* 265:35–40. <https://doi.org/10.1111/j.1574-6968.2006.00463.x>.
68. Grijpstra J, Arenas J, Rutten L, Tommassen J. 2013. Autotransporter secretion: varying on a theme. *Res Microbiol* 164:562–582. <https://doi.org/10.1016/j.resmic.2013.03.010>.
69. Desvaux M, Parham NJ, Henderson IR. 2004. The autotransporter secretion system. *Res Microbiol* 155:53–60. <https://doi.org/10.1016/j.resmic.2003.10.002>.
70. Jacob-Dubuisson F, Fernandez R, Coutte L. 2004. Protein secretion through autotransporter and two-partner pathways. *Biochim Biophys Acta* 1694:235–257. <https://doi.org/10.1016/j.bbamcr.2004.03.008>.
71. van Dooren SJ, Tame JR, Luirink J, Oudega B, Otto BR. 2001. Purification of the autotransporter protein Hbp of *Escherichia coli*. *FEMS Microbiol Lett* 205:147–150. <https://doi.org/10.1111/j.1574-6968.2001.tb10938.x>.
72. Richard KL, Kelley BR, Johnson JG. 2019. Heme uptake and utilization by gram-negative bacterial pathogens. *Front Cell Infect Microbiol* 9:81. <https://doi.org/10.3389/fcimb.2019.00081>.
73. Parker MW, Postma JP, Pattus F, Tucker AD, Tsernoglou D. 1992. Refined structure of the pore-forming domain of colicin A at 2.4 Å resolution. *J Mol Biol* 224:639–657. [https://doi.org/10.1016/0022-2836\(92\)90550-4](https://doi.org/10.1016/0022-2836(92)90550-4).
74. Parker MW, Pattus F, Tucker AD, Tsernoglou D. 1989. Structure of the membrane-pore-forming fragment of colicin A. *Nature* 337:93–96. <https://doi.org/10.1038/337093a0>.
75. Dal Peraro M, van der Goot FG. 2016. Pore-forming toxins: ancient, but never really out of fashion. *Nat Rev Microbiol* 14:77–92. <https://doi.org/10.1038/nrmicro.2015.3>.
76. Prados-Rosales R, Weinrick BC, Pique DG, Jacobs WR, Jr, Casadevall A, Rodriguez GM. 2014. Role for *Mycobacterium tuberculosis* membrane vesicles in iron acquisition. *J Bacteriol* 196:1250–1256. <https://doi.org/10.1128/JB.01090-13>.
77. Layre E. 2020. Trafficking of *Mycobacterium tuberculosis* envelope components and release within extracellular vesicles: host-pathogen interactions beyond the wall. *Front Immunol* 11:1230. <https://doi.org/10.3389/fimmu.2020.01230>.
78. Chiplunkar SS, Silva CA, Bermudez LE, Danelishvili L. 2019. Characterization of membrane vesicles released by *Mycobacterium avium* in response to environment mimicking the macrophage phagosome. *Future Microbiol* 14:293–313. <https://doi.org/10.2217/fmb-2018-0249>.
79. Prados-Rosales R, Baena A, Martinez LR, Luque-Garcia J, Kalscheuer R, Veeraraghavan U, Camara C, Nosanchuk JD, Besra GS, Chen B, Jimenez J, Glatman-Freedman A, Jacobs WR, Jr, Porcelli SA, Casadevall A. 2011. *Mycobacteria* release active membrane vesicles that modulate immune responses in a TLR2-dependent manner in mice. *J Clin Invest* 121:1471–1483. <https://doi.org/10.1172/JCI44261>.
80. Lee J, Kim SH, Choi DS, Lee JS, Kim DK, Go G, Park SM, Kim SH, Shin JH, Chang CL, Gho YS. 2015. Proteomic analysis of extracellular vesicles derived from *Mycobacterium tuberculosis*. *Proteomics* 15:3331–3337. <https://doi.org/10.1002/pmic.201500037>.
81. Siroy A, Mailaender C, Harder D, Koerber S, Wolschendorf F, Danilchanka O, Wang Y, Heinz C, Niederweis M. 2008. Rv1698 of *Mycobacterium tuberculosis* represents a new class of channel-forming outer membrane proteins. *J Biol Chem* 283:17827–17837. <https://doi.org/10.1074/jbc.M800866200>.
82. Danilchanka O, Sun J, Pavlenok M, Maueroder C, Speer A, Siroy A, Marrero J, Trujillo C, Mayhew DL, Doornbos KS, Munoz LE, Herrmann M, Ehrt S, Berens C, Niederweis M. 2014. An outer membrane channel protein of *Mycobacterium tuberculosis* with exotoxin activity. *Proc Natl Acad Sci U S A* 111:6750–6755. <https://doi.org/10.1073/pnas.1400136111>.
83. Arora A, Rinehart D, Szabo G, Tamm LK. 2000. Refolded outer membrane protein A of *Escherichia coli* forms ion channels with two conductance states in planar lipid bilayers. *J Biol Chem* 275:1594–1600. <https://doi.org/10.1074/jbc.275.3.1594>.
84. Prilipov A, Phale PS, Koebnik R, Widmer C, Rosenbusch JP. 1998. Identification and characterization of two quiescent porin genes, *nmpC* and *ompN*, in *Escherichia coli* BE. *J Bacteriol* 180:3388–3392. <https://doi.org/10.1128/JB.180.13.3388-3392.1998>.
85. Conlan S, Zhang Y, Cheley S, Bayley H. 2000. Biochemical and biophysical characterization of OmpG: a monomeric porin. *Biochemistry* 39:11845–11854. <https://doi.org/10.1021/bi001065h>.
86. Dahan D, Vachon V, Laprade R, Coulton JW. 1994. Voltage gating of porins from *Haemophilus influenzae* type b. *Biochim Biophys Acta* 1189:204–211. [https://doi.org/10.1016/0005-2736\(94\)90067-1](https://doi.org/10.1016/0005-2736(94)90067-1).
87. Dulberger CL, Rubin EJ, Boutte CC. 2020. The mycobacterial cell envelope—a moving target. *Nat Rev Microbiol* 18:47–59. <https://doi.org/10.1038/s41579-019-0273-7>.
88. Ekiert DC, Cox JS. 2014. Structure of a PE-PPE-EspG complex from *Mycobacterium tuberculosis* reveals molecular specificity of ESX protein secretion. *Proc Natl Acad Sci U S A* 111:14758–14763. <https://doi.org/10.1073/pnas.1409345111>.
89. Cox J, Mann M. 2008. MaxQuant enables high peptide identification rates, individualized p.p.b.-range mass accuracies and proteome-wide protein quantification. *Nat Biotechnol* 26:1367–1372. <https://doi.org/10.1038/nbt.1511>.
90. Cox J, Hein MY, Luber CA, Paron I, Nagaraj N, Mann M. 2014. Accurate proteome-wide label-free quantification by delayed normalization and maximal peptide ratio extraction, termed MaxLFQ. *Mol Cell Proteomics* 13:2513–2526. <https://doi.org/10.1074/mcp.M113.031591>.
91. Tyanova S, Temu T, Sinitcyn P, Carlson A, Hein MY, Geiger T, Mann M, Cox J. 2016. The Perseus computational platform for comprehensive analysis of (prote)omics data. *Nat Methods* 13:731–740. <https://doi.org/10.1038/nmeth.3901>.
92. Zakharian E, Reusch RN. 2006. Pore characteristics of nontypeable *Haemophilus influenzae* outer membrane protein P5 in planar lipid bilayers. *Biophys J* 91:3242–3248. <https://doi.org/10.1529/biophysj.106.088781>.